ASTRONOMY

Water heavily fractionated as it ascends on Mars as revealed by ExoMars/NOMAD

Geronimo L. Villanueva[1]*, Giuliano Liuzzi[1,2], Matteo M. J. Crismani[3,4], Shohei Aoki[5,6], Ann Carine Vandaele[4], Frank Daerden[4], Michael D. Smith[1], Michael J. Mumma[1], Elise W. Knutsen[1,2], Lori Neary[5], Sebastien Viscardy[5], Ian R. Thomas[5], Miguel Angel Lopez-Valverde[7], Bojan Ristic[5], Manish R. Patel[8], James A. Holmes[8], Giancarlo Bellucci[9], Jose Juan Lopez-Moreno[7], NOMAD team†

Isotopic ratios and, in particular, the water D/H ratio are powerful tracers of the evolution and transport of water on Mars. From measurements performed with ExoMars/NOMAD, we observe marked and rapid variability of the D/H along altitude on Mars and across the whole planet. The observations (from April 2018 to April 2019) sample a broad range of events on Mars, including a global dust storm, the evolution of water released from the southern polar cap during southern summer, the equinox phases, and a short but intense regional dust storm. In three instances, we observe water at very high altitudes (>80 km), the prime region where water is photodissociated and starts its escape to space. Rayleigh distillation appears the be the driving force affecting the D/H in many cases, yet in some instances, the exchange of water reservoirs with distinctive D/H could be responsible.

INTRODUCTION

Mars shows a scarred landscape carved by a wet past [e.g., (*1*)], yet it is not clear how much of this water ran across the Martian surface or for how long. The debate includes considerations of a wet and cold past scenario [e.g., (*2*)], wet and hot past [e.g., (*3*)], or hybrid models [e.g., (*4*)]. In many cases, these scenarios are stimulated by the strong geological record but depend highly on the assumed atmospheric states and escape considerations. Measurements of isotopic ratios and, in particular, the deuterium to hydrogen ratio (D/H) in water provide a powerful method to constrain volatile escape [e.g., (*5*)] and to track the transport of water between reservoirs (e.g., seasonal transport between the polar caps). Because the thermal "Jeans" escape rates for each isotope are different (larger for the lighter forms), over long periods, the atmosphere becomes enriched in the heavy isotopic forms. By mapping the current isotopic ratios, one can also test for the existence of different volatile reservoirs (e.g., polar caps and regolith) with distinct isotopic signatures (*6*).

The idea of distinct water reservoirs interacting during the water cycle was strengthened by the strong isotopic variations in the water column that were observed across the planet via ground-based astronomy (*5*, *7*). Nevertheless, the D/H ratio is also heavily affected by climatological processes because the vapor pressures of HDO and H_2O differ near the freezing point, making the condensation/sublimation cycle of the isotopologs sensitive to local temperatures, to saturation levels, and to the presence of aerosol condensation nuclei. This would lead to strong seasonal D/H gradients, while local orography and cloud formation would lead to longitudinal variability.

MATERIALS AND METHODS

By performing high-resolution infrared spectroscopic observations across the entire planet, the ExoMars Trace Gas Orbiter (TGO) provides an unprecedented view of the three-dimensional structure and composition of the Martian atmosphere. Specifically, the NOMAD (Nadir and Occultation for Mars Discovery) (*8*, *9*) instrument suite aboard TGO has the capability to provide vertical profiles and global maps of water (both H_2O and HDO), water ice, and dust using high-resolution infrared spectroscopy. The vertical and seasonal trends in water vapor during the global and regional dust storms of Mars Year (MY) 34 were extensively presented (*10*), while the present work emphasizes the relationship between water abundance and the D/H ratio based on data acquired with the SO (solar occultation) channel of NOMAD between April 2018 (the start of science operations) and April 2019. This interval corresponds to $L_s = 162.5°$ of MY 34 to $L_s = 15.0°$ of MY 35 and included the "global dust storm" (GDS) that engulfed the planet in MY 34 (June to September 2018). A total of 219,464 individual SO spectra through the Martian atmosphere were collected during 1920 occultation events.

ExoMars TGO's near-polar orbit with up to 24 occultations per sol, shared between NOMAD and Atmospheric Chemistry Suite (*11*), permits high-cadence mapping of the variability of water and D/H over time. Sensitivity typically allows water mapping up to an altitude of ~100 km for the main isotopolog of water (H_2O) and up to ~50 km for HDO and, thus, D/H (with a typical resolution of ~1 km), while high opacity from aerosols and airborne dust restrict the lower boundary to 5 to 10 km. The SO channel operates at wavelengths between 2.2 and 4.3 μm (2325 to 4500 cm^{-1}) using an echelle grating, combined with an acousto-optic tunable filter (AOTF) and delivers a spectral resolving power of ~20,000. The width of each AOTF filtered order varies from 20 to 35 cm^{-1}, linearly increasing with the diffraction order number. The infrared channels (SO and nadir channel) of the NOMAD instrument are described in detail in previous works (*12*–*15*), while a complete calibration using the in-flight data acquired before the science phase has been discussed in depth (*16*).

---

[1]NASA Goddard Space Flight Center, Greenbelt, MD, USA. [2]Department of Physics, American University, Washington, DC, USA. [3]NPP/USRA, Goddard Space Flight Center, Greenbelt, MD, USA. [4]California State University, San Bernardino, Department of Physics, CA USA. [5]Royal Belgian Institute for Space Aeronomy, Brussels, Belgium. [6]University of Liege, Liege, Belgium. [7]Instituto de Astrofísica de Andalucía, Granada, Spain. [8]Open University, Milton Keynes UK. [9]Istituto di Astrofisica e Planetologia, Rome, Italy.
*Corresponding author. Email: geronimo.villanueva@nasa.gov
†See section S2 in the Supplementary Materials.

During an occultation, the SO instrument is pointed toward the Sun to observe the solar radiation as attenuated by the Martian atmosphere at different altitudes, enabling an investigation of the atmospheric vertical structure. On a typical occultation, five or six different diffraction orders are sampled at 1-s intervals, with H_2O sampled in two or more diffraction orders and HDO in one of them, ultimately allowing quantification of D/H for almost all NOMAD occultations (see example spectra in Fig. 1). The possibility to access different absorption bands of water is of great benefit to achieve measurement accuracy throughout a vast range of altitudes since absorption regimes vary with the observed atmospheric column. For instance, strong fundamental bands of H_2O (such as the ν_3 band at 2.7 μm, orders 168 to 170) probe water up to 120 km but become saturated at ~50 km, while the weaker $2\nu_2$ band at 3.3 μm (orders 133 to 136) probes deeper into the atmosphere without saturation.

We derived H_2O and HDO slant column densities from the resulting spectra by using Goddard's Planetary Spectrum Generator (PSG) (*17*), which is based on an optimal estimation approach (*18*), modified with an extra regularization parameter (*19*, *20*). For Mars, PSG ingests a specific line compilation for water and its isotopologs, tailored for a CO_2-rich atmosphere (*21*, *22*). The derivation of molecular mixing ratios does depend on the assumed pressure/temperature profiles, and in particular, the local atmospheric density and temperature can vary during perihelion season, depending on the intensity of heating introduced by dust present in the atmosphere. Because portions of the dataset were acquired during the GDS, the a priori atmospheric state has to be representative of those specific conditions. We calculated that using the Global Environmental Multiscale (GEM)–Mars model (*23*, *24*) and a specific dust storm scenario that reproduces the dust state of the atmosphere during MY 34. The properties of the GEM-Mars GDS model during the storm differ substantially from the average climatology of the Mars Climate Database (v5.2) (*25*), with temperature deviations as large as 30 K modeled in the middle atmosphere (fig. S4). The largest discrepancies are found in the southern hemisphere, where dust concentrations are greater during the GDS. The dust abundance or the assumed aerosols profiles do not affect the H_2O and HDO SO retrievals directly (only when the atmosphere is fully optically thick). Dust will tend to heat the atmosphere, and that may reflect in enhanced partition functions, which ultimately affect the retrieved molecular densities. On the other hand, this effect is particularly small for the retrieved D/H since both partition functions vary similarly to temperature, so this systematic effect is removed when computing D/H.

To compute a single molecular profile per occultation, measurements are first collected to form a single dataset colocated in altitude (typically one to two orders for H_2O and one to two orders for HDO) and then aggregated by a weighted mean. Each molecular retrieval is assumed to be independent from the nearby altitude retrievals, with the resulting uncertainty also including the standard deviation of the measurements (see figs. S6 and S7). The D/H ratio is determined using the same approach: For each occultation and altitude, the D/H is computed using the weighted averages of H_2O and HDO. Uncertainties were computed using standard optimal estimation statistics that are further corrected for the quality of the residual spectra (chi-square of the fit). Measurements from several orders and computation of uncertainties of D/H were performed using standard error propagation methods [see also (*5*, *9*)].

RESULTS

The retrievals were organized by season and latitude to investigate the main processes acting on water and D/H. As shown in Fig. 2, the water vapor abundances change markedly across the year, with D/H also showing important changes. Previous measurements of water columns [e.g., (*26*–*30*)] also report great seasonal, temporal, and spatial variability, with strong enhancements during the summer hemisphere as reported here. The seasonal variability reported here should be viewed with caution since the orbit of ExoMars causes seasonal and latitude changes to be convolved (Fig. 2, top). Note that these are local D/H values at a specific altitude (not of the column), and they can be only understood in the context of the local climatology at this specific altitude/latitude/longitude/season.

Consistent with earlier studies of dust storms (*10*, *31*), we found that water vapor abundances in the middle atmosphere (40 to 100 km) increased substantially during the GDS (June to mid-September 2018) and the regional dust storm of January 2019. In particular, water vapor reaches very high altitudes, at least 100 km, during the GDS. A General Circulation Model simulation explained that dust

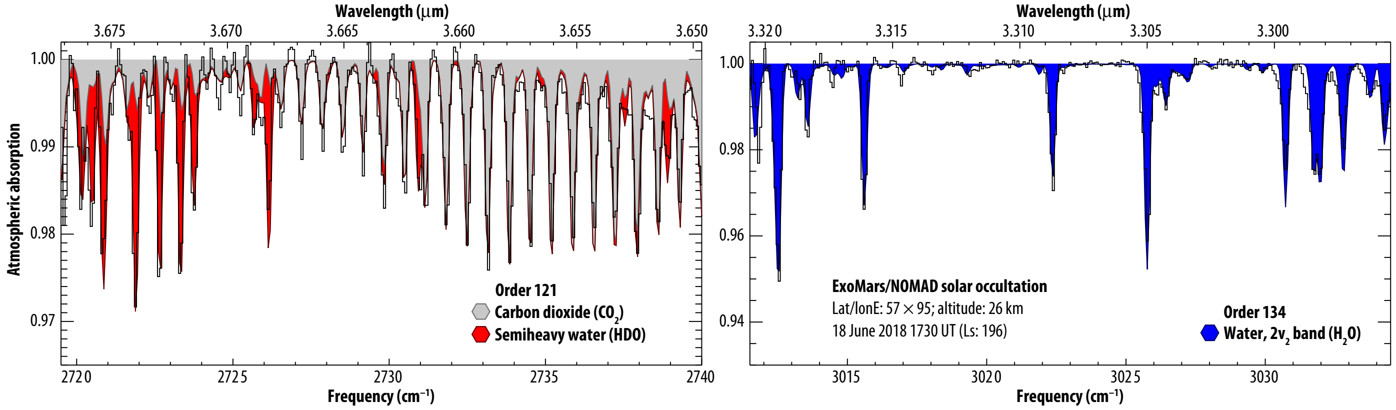

Fig. 1. Representative spectra of the main NOMAD orders used to sample HDO (left) and H_2O (right) taken on June 2018 for a SO altitude of 26 km. The observations were taken during the GDS and show that the two bands (ν_1 of HDO and $2\nu_2$ of H_2O) have similar opacities and, therefore, comparable curves of growth and altitude sensitivity.

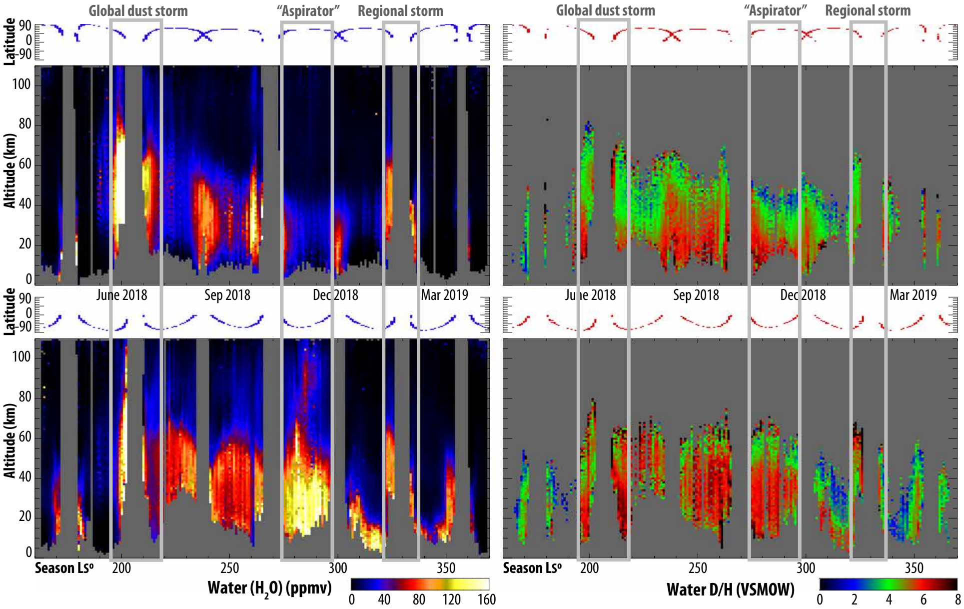

Fig. 2. Seasonal variability of water (left) and the D/H (right) for the northern hemisphere (top) and the southern hemisphere (bottom). Only H_2O values with sigmas lower than 15 parts per million by volume (ppmv) and D/H values with sigmas lower than 0.8 VSMOW are shown (point-by-point error bars are presented in fig. S7). Because of the ExoMars/TGO orbit, there is an intrinsic relationship between the seasonal and latitudinal sampling for the occultations, and the latitude subpanels indicate which latitudes are sampled during a particular instance. Water is observed to reach the upper regions of the atmosphere (>80 km) during indicated events: (i) during the GDS, (ii) during the regional dust storm, and (ii) during southern summer, in which we observe a localized upper atmosphere water excess.

storm–related increases in atmospheric temperatures elevate the hygropause, hence reducing ice cloud formation and so allowing water vapor to extend into the middle atmosphere (*24*). We confirm that (i) water vapor also reaches very high altitudes during the southern summer solstice, independently of dust storms [see lower dust content during this period as reported in (*32*)] and (ii) that water drops to very low values at high/low latitudes and close to equinox with the hygropause subsiding to a few scale heights. With regard to D/H, we observe the following distinct features: (i) the D/H ratio is typically ~6 VSMOW (Vienna Standard Mean Ocean Water) in the lower atmosphere, (ii) the D/H ratio decreases with altitude, as observed similarly on Earth (*22*), and (iii) the D/H ratio is low (2 to 4 VSMOW) at high/low latitudes and close to equinox where H_2O is low.

Within half an MY, we observed three instances (the GDS, southern summer, and the regional dust storm) of water vapor reaching the upper atmosphere, where it can be readily photolyzed (*24*), bypassing the traditional H_2 diffusion limitations on water escape rates (*33*). The D/H ratio is probably quite low at these high altitudes if we attempted to extrapolate our D/H values to 70 to 80 km from the low/middle atmosphere (50 to 60 km), yet photolysis, vertical transport, and other processes may lead to great variability at these altitudes. On Earth, mesospheric D/H measurements show strong variability (*34*), which has been attributed to the differential photolysis rates of HDO and H_2O combined with atmospheric transport and CH_4/CH_3D photochemistry. For the lower atmosphere, the decrease of the D/H with altitude can be explained, as on Earth, by Rayleigh fractionation (*22*). The fractionation in the troposphere of Earth has been shown to be also strongly dependent on atmospheric dynamics [e.g., see convective/subsiding results in (*35*) and formation of clouds and atmospheric microphysics in (*36*)], resulting in highly variable deuterium enrichments with respect to altitude, time, and position on the planet [e.g., (*37*, *38*)]. These may explain the localized behavior and variability in the D/H ratio observed across Mars, and it is consistent with the column variability observed in (*5*).

To explore the 3D structure of the water cycle and the D/H signatures, we aggregated the data into seasonal periods and computed latitude versus altitude plots of water vapor and D/H (Fig. 3). These plots show a marked variability of the vertical profiles of water and D/H, with clear and defined latitudinal structures. As also shown in (*10*), the increase of the water vapor abundances at higher altitudes is remarkable for the global (L_s = 190° to 210°) and regional dust storm (L_s = 320° to 330°), yet this excess water is only confined to equatorial and mid-latitudes (<60°). Although the atmosphere is filled with water to high altitudes during these times, the D/H remains relatively low (4 to 5 VSMOW) and increases to ~6 VSMOW only at high latitudes (away from the subsolar point) and low altitudes. In principle, this is expected and could be an indication of Rayleigh fractionation and cloud formation (*9*), where D/H is actually decreasing with altitude, but it is only measured with sufficient signal-to-noise ratio (low opacities) at high altitudes (>40 km) in mid-latitudes and at low altitudes (10 to 40 km) in high latitudes.

The injection of southern polar cap water with enhanced D/H is clearly seen as southern spring progresses to summer. Between L_s = 270° and 300°, we see water vapor increasing in the southern hemisphere and also in altitude as we approach the polar latitudes [labeled in Fig. 2 as "aspirator" (from the Latin word "aspire" to "rise, climb up")]. The D/H remains high (>6 VSMOW) for most of this water (probably coming from the seasonal southern polar cap) and decreases to <4 VSMOW at higher altitudes. Fractionation is also present at this season, associated with a more compact hygropause in the colder/winter hemisphere and a more compact D/H profile. As we move to southern fall (L_s = 300° to 320°), the water may have been transported

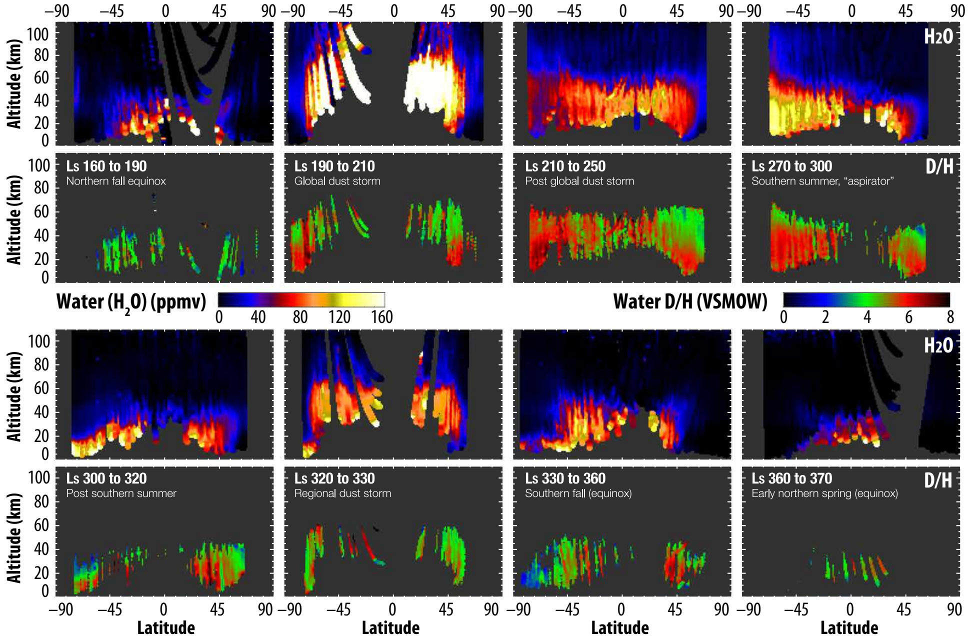

Fig. 3. Latitudinal variability of water and D/H across the seasons, sampling two equinoxes, a solstice, a global and a regional dust storm, and the injection of water into the atmosphere from the southern polar cap during southern summer. Only H_2O values with sigmas lower than 15 ppmv and D/H values with sigmas lower than 1.5 VSMOW are shown. The panels clearly show the evolution of the water cycle across these complex events, revealing marked changes in the water and D/H distributions across the events. The sparsity of valid D/H datasets considering this fine temporal sampling does not allow us to fully capture every detail of the latitude by altitude variability, yet two points are clearly observed: (i) The water released from the southern polar cap has a distinctive 6- to 7-VSMOW enrichment in D/H, and (ii) during southern fall (Ls 300 to 320 and Ls 330 to 360), the hygropause is compacted in the southern hemisphere, leading also to very low D/H at these latitudes and season.

to equatorial latitudes, which is then puffed into higher altitudes during the regional dust storm (L_s = 320° to 330°). During the regional storm, water reaches only 60 km in altitude, in comparison to 80 to 100 km observed during the GDS. Water abundance then collapses to low values and at low altitudes during southern fall (L_s = 330° to 360°) and early northern spring (L_s = 360° to 370°, MY 34). The D/H information during this period is inconclusive since water is confined to low-altitude layers of the atmosphere, where long atmospheric path lengths prevent observations of HDO with sufficient sensitivity due to aerosol extinction. During this season, we do observe low D/H values in the southern hemisphere and very low values at low altitudes.

DISCUSSION

Multiple reservoirs have been identified to account for the current inventory of water on Mars, ranging from the observable polar layered deposits (*39*, *40*) to ice-rich regolith at mid-latitudes (*41*, *42*), near-surface reservoirs at high latitudes (*43*), and subsurface reservoirs, as implied by gamma ray and neutron observations (*44*). If each of these reservoirs has a distinct isotopic content, then the signature of the exchange between these reservoirs should be present in the observed atmospheric D/H ratio variation. The outstanding question is whether each reservoir has or should have a distinct isotopic signature. The fact that Mars has had marked variations in its obliquity (*45*), changing from ~45° to 15° in the last million years, would suggest that the polar caps are relatively new and that all the water reservoirs should have been "mixed" within the last 10 million years. Considering that it takes billions of years for notable changes in the D/H ratio to take effect, the different reservoirs may have the same isotopic signature, yet this hypothesis assumes that all labile water is mixed by the hydrological cycle. A testable way to prove this hypothesis would be to ultimately probe the water D/H in the polar caps below the seasonal layers. We then ask, is the variability that we observe related to different reservoirs?

As on Earth (*46*), D/H on Mars shows great variability in time and space, consistent with previous column integrated reports in (*5*, *47*). Observations using SOFIA (Stratospheric Observatory for Infrared Astronomy) at thermal wavelengths (*48*) do also report variability yet much more subdued. Thermal observations are more affected by the assumed temperature profiles and thermal contrast, and the spatial resolution of SOFIA observations is typically only four to five pixels across Mars' disk; however, it is interesting to note this difference between SOFIA and other results. In particular, there may be an annual element to this hemispheric variability of the observed D/H column. Strong isotopic anomalies are typically observed at regions with strong temperature/water gradients, like the polar caps, and these are typically hard to capture and sample at moderate spatial resolutions from the ground.

In many cases, the observed variations of the D/H across seasons and with altitude revealed by our work could be attributed to Rayleigh fractionation and cloud formation (*32*), with the D/H decreasing with altitude and dropping or decreasing at the edge of the hygropause. In the zonal mean Fig. 3, the seasonal water being added from the southern polar cap during southern summer (L_s = 210° to 250° and 270° to 300°) has a ~6- to 7-VSMOW value, consistent with the column values measured in (*5*) for the northern pole water. This would perhaps mean that the two main reservoirs of water on Mars, the polar caps, share a common value of D/H, yet the south polar cap only has seasonal water ice, not permanent. The lower values in D/H observed during southern fall (L_s = 300° to 320° and 330° to 360°) at the southern latitudes would imply that a large fraction of the HDO was sequestered. This could be associated to be a rapid collapse of the hygropause at these latitudes, which leads to a steep Rayleigh fractionation condensation profile. The existence of water ice clouds during this period and season (*31*, *32*) is consistent with this view.

Further interpreting the results, in particular, the concept of multiple reservoirs of water with a distinctive D/H and water escape would require detailed comparisons with a highly parameterized weather and climate model. The model would need to have a comparable prescription of the water and aerosol distribution and to have a realistic heterogenous water fractionation model to fully capture the observed D/H variability and advance current models (*49*–*51*). The ultimate question is then what is the representative D/H of labile water on Mars right now? If we assume that the observed fractionation is driven mainly by Rayleigh distillation, then the observed maximum D/H values of 6 to 7 VSMOW observed in this work are then descriptive of the truly intrinsic water D/H when both isotopologs are fully vaporized. This value is consistent with previous findings as reported above and would further establish that Mars has lost a substantial amount of water (>137-m global equivalent layer) (*5*). The fact that we observe three instances during a single MY where water is brought to the upper regions of the atmosphere (>60 km; Figs. 2 and 3) would provide the means for this escape to take place.

SUPPLEMENTARY MATERIALS

Supplementary material for this article is available at http://advances.sciencemag.org/cgi/content/full/7/7/eabc8843/DC1

REFERENCES AND NOTES

1. M. H. Carr, J. W. Head III, Oceans on Mars: An assessment of the observational evidence and possible fate. *J. Geophys. Res.* **108**, 5042 (2003).
2. A. G. Fairén, A cold and wet Mars. *Icarus* **208**, 165–175 (2010).
3. J. M. Davis, M. Balme, P. M. Grindrod, R. M. E. Williams, S. Gupta, Extensive Noachian fluvial systems in Arabia Terra: Implications for early Martian climate. *Geology* **44**, 847–850 (2016).
4. K. M. Cannon, S. W. Parman, J. F. Mustard, Primordial clays on Mars formed beneath a steam or supercritical atmosphere. *Nature* **552**, 88–91 (2017).
5. G. L. Villanueva, M. J. Mumma, R. E. Novak, H. U. Käufl, P. Hartogh, T. Encrenaz, A. Tokunaga, A. Khayat, M. D. Smith, Strong water isotopic anomalies in the martian atmosphere: Probing current and ancient reservoirs. *Science* **348**, 218–221 (2015).
6. D. Fisher, R. E. Novak, M. J. Mumma, D/H ratio during the northern polar summer and what the Phoenix mission might measure. *J. Geophys. Res.* **113**, E00A15 (2008).
7. R. E. Novak, M. J. Mumma, G. L. Villanueva, Measurement of the isotopic signatures of water on Mars; implications for studying methane. *Planet. Space Sci.* **59**, 163–168 (2011).
8. A. C. Vandaele, J. J. López-Moreno, M. R. Patel, G. Bellucci, F. Daerden, R. Drummond, E. Neefs, S. Robert, J. Rodriguez Gomez, NOMAD, a spectrometer suite for nadir and solar occultation observations on the ExoMars Trace Gas Orbiter. *EGU Gen. Assem. 2012* **14**, 3362 (2012).
9. A. C. Vandaele, O. Korablev, F. Daerden, S. Aoki, I. R. Thomas, F. Altieri, M. López-Valverde, G. Villanueva, G. Liuzzi, M. D. Smith, J. T. Erwin, L. Trompet, A. A. Fedorova, F. Montmessin, A. Trokhimovskiy, D. A. Belyaev, N. I. Ignatiev, M. Luginin, K. S. Olsen, L. Baggio, J. Alday, J.-L. Bertaux, D. Betsis, D. Bolsée, R. T. Clancy, E. Cloutis, C. Depiesse, B. Funke, M. Garcia-Comas, J.-C. Gérard, M. Giuranna, F. Gonzalez-Galindo, A. V. Grigoriev, Y. S. Ivanov, J. Kaminski, O. Karatekin, F. Lefèvre, S. Lewis, M. López-Puertas, A. Mahieux, I. Maslov, J. Mason, M. J. Mumma, L. Neary, E. Neefs, A. Patrakeev, D. Patsaev, B. Ristic, S. Robert, F. Schmidt, A. Shakun, N. A. Teanby, S. Viscardy, Y. Willame, J. Whiteway, V. Wilquet, M. J. Wolff, G. Bellucci, M. R. Patel, J.-J. López-Moreno, F. Forget, C. F. Wilson, H. Svedhem, J. L. Vago, D. Rodionov; NOMAD Science Team; ACS Science Team, Martian dust storm impact on atmospheric H_2O and D/H observed by ExoMars Trace Gas Orbiter. *Nature* **568**, 521–525 (2019).
10. S. Aoki, A. C. Vandaele, F. Daerden, G. L. Villanueva, G. Liuzzi, I. R. Thomas, J. T. Erwin, L. Trompet, S. Robert, L. Neary, S. Viscardy, R. T. Clancy, M. D. Smith, M. A. Lopez-Valverde, B. Hill, B. Ristic, M. R. Patel, G. Bellucci, J.-J. Lopez-Moreno; NOMAD Team, Water vapor vertical profiles on Mars in dust storms observed by TGO/NOMAD. *J. Geophys. Res. Planets* **124**, 3482–3497 (2019).
11. O. Korablev, F. Montmessin, A. Trokhimovskiy, A. A. Fedorova, A. V. Shakun, A. V. Grigoriev, B. E. Moshkin, N. I. Ignatiev, F. Forget, F. Lefèvre, K. Anufreychik, I. Dzuban, Y. S. Ivanov, Y. K. Kalinnikov, T. O. Kozlova, A. Kungurov, V. Makarov, F. Martynovich, I. Maslov, D. Merzlyakov, P. P. Moiseev, Y. Nikolskiy, A. Patrakeev, D. Patsaev, A. Santos-Skripko, O. Sazonov, N. Semena, A. Semenov, V. Shashkin, A. Sidorov, A. V. Stepanov, I. Stupin, D. Timonin, A. Y. Titov, A. Viktorov, A. Zharkov, F. Altieri, G. Arnold, D. A. Belyaev, J. L. Bertaux, D. S. Betsis, N. Duxbury, T. Encrenaz, T. Fouchet, J.-C. Gérard, D. Grassi, S. Guerlet, P. Hartogh, Y. Kasaba, I. Khatuntsev, V. A. Krasnopolsky, R. O. Kuzmin, E. Lellouch, M. A. Lopez-Valverde, M. Luginin, A. Määttänen, E. Marcq, J. Martin Torres, A. S. Medvedev, E. Millour, K. S. Olsen, M. R. Patel, C. Quantin-Nataf, A. V. Rodin, V. I. Shematovich, I. Thomas, N. Thomas, L. Vazquez, M. Vincendon, V. Wilquet, C. F. Wilson, L. V. Zasova, L. M. Zelenyi, M. P. Zorzano, The Atmospheric Chemistry Suite (ACS) of three spectrometers for the ExoMars 2016 trace gas orbiter. *Space Sci. Rev.* **214**, 7 (2018).
12. A. C. Vandaele, E. Neefs, R. Drummond, I. R. Thomas, F. Daerden, J.-J. Lopez-Moreno, J. Rodriguez, M. R. Patel, G. Bellucci, M. Allen, F. Altieri, D. Bolsée, T. Clancy, S. Delanoye, C. Depiesse, E. Cloutis, A. Fedorova, V. Formisano, B. Funke, D. Fussen, A. Geminale, J.-C. Gérard, M. Giuranna, N. Ignatiev, J. Kaminski, O. Karatekin, F. Lefèvre, M. López-Puertas, M. López-Valverde, A. Mahieux, J. McConnell, M. Mumma, L. Neary, E. Renotte, B. Ristic, S. Robert, M. Smith, S. Trokhimovsky, J. V. Auwera, G. Villanueva, J. Whiteway, V. Wilquet, M. Wolff, Science objectives and performances of NOMAD, a spectrometer suite for the ExoMars TGO mission. *Planet. Space Sci.* **119**, 233–249 (2015).
13. A. C. Vandaele, J.-J. Lopez-Moreno, M. R. Patel, G. Bellucci, F. Daerden, B. Ristic, S. Robert, I. R. Thomas, V. Wilquet, M. Allen, G. Alonso-Rodrigo, F. Altieri, S. Aoki, D. Bolsée, T. Clancy, E. Cloutis, C. Depiesse, R. Drummond, A. Fedorova, V. Formisano, B. Funke, F. González-Galindo, A. Geminale, J.-C. Gérard, M. Giuranna, L. Hetey, N. Ignatiev, J. Kaminski, O. Karatekin, Y. Kasaba, M. Leese, F. Lefèvre, S. R. Lewis, M. López-Puertas, M. López-Valverde, A. Mahieux, J. Mason, J. McConnell, M. Mumma, L. Neary, E. Neefs, E. Renotte, J. Rodriguez-Gomez, G. Sindoni, M. Smith, A. Stiepen, A. Trokhimovsky, J. V. Auwera, G. Villanueva, S. Viscardy, J. Whiteway, Y. Willame, M. Wolff, NOMAD, an integrated suite of three spectrometers for the ExoMars trace gas mission: Technical description, science objectives and expected performance. *Space Sci. Rev.* **214**, 80 (2018).
14. E. Neefs, A. C. Vandaele, R. Drummond, I. R. Thomas, S. Berkenbosch, R. Clairquin, S. Delanoye, B. Ristic, J. Maes, S. Bonnewijn, G. Pieck, E. Equeter, C. Depiesse, F. Daerden, E. V. Ransbeeck, D. Nevejans, J. Rodriguez-Gómez, J.-J. López-Moreno, R. Sanz, R. Morales, G. P. Candini, M. C. Pastor-Morales, B. A. del Moral, J.-M. Jeronimo-Zafra, J. M. Gómez-López, G. Alonso-Rodrigo, I. Pérez-Grande, J. Cubas, A. M. Gomez-Sanjuan, F. Navarro-Medina, T. Thibert, M. R. Patel, G. Bellucci, L. De Vos, S. Lesschaeve, N. V. Vooren, W. Moelans, L. Aballea, S. Glorieux, A. Baeke, D. Kendall, J. De Neef, A. Soenen, P.-Y. Puech, J. Ward, J.-F. Jamoye, D. Diez, A. Vicario-Arroyo, M. Jankowski, NOMAD spectrometer on the ExoMars trace gas orbiter mission: Part 1—Design, manufacturing and testing of the infrared channels. *Appl. Optics* **54**, 8494–8520 (2015).
15. I. R. Thomas, A. C. Vandaele, S. Robert, E. Neefs, R. Drummond, F. Daerden, S. Delanoye, B. Ristic, S. Berkenbosch, R. Clairquin, J. Maes, S. Bonnewijn, C. Depiesse, A. Mahieux, L. Trompet, L. Neary, Y. Willame, V. Wilquet, D. Nevejans, L. Aballea, W. Moelans, L. De Vos, S. Lesschaeve, N. Van Vooren, J.-J. Lopez-Moreno, M. R. Patel, G. Bellucci; NOMAD Team, Optical and radiometric models of the NOMAD instrument part II: The infrared channels – SO and LNO. *Opt. Express* **24**, 3790–3805 (2016).
16. G. Liuzzi, G. L. Villanueva, M. J. Mumma, M. D. Smith, F. Daerden, B. Ristic, I. Thomas, A. C. Vandaele, M. R. Patel, J.-J. Lopez-Moreno, G. Bellucci, Methane on Mars: New insights into the sensitivity of CH4 with the NOMAD/ExoMars spectrometer through its first in-flight calibration. *Icarus* **321**, 671–690 (2019).
17. G. L. Villanueva, M. D. Smith, S. Protopapa, S. Faggi, A. M. Mandell, Planetary spectrum generator: An accurate online radiative transfer suite for atmospheres, comets, small bodies and exoplanets. *J. Quant. Spectrosc. Radiat. Transf.* **217**, 86–104 (2018).
18. C. D. Rodgers, *Inverse Methods for Atmospheric Sounding* (series on Atmospheric, Oceanic and Planetary Physics, World Scientific, 2000); www.worldscientific.com/worldscibooks/10.1142/3171.
19. G. Liuzzi, G. Masiello, C. Serio, S. Venafra, C. Camy-Peyret, Physical inversion of the full IASI spectra: Assessment of atmospheric parameters retrievals, consistency of spectroscopy and forward modelling. *J. Quant. Spectrosc. Radiat. Transf.* **182**, 128–157 (2016).
20. A. Carissimo, I. De Feis, C. Serio, The physical retrieval methodology for IASI: The δ-IASI code. *Environ. Model. Software* **20**, 1111–1126 (2005).
21. I. E. Gordon, L. S. Rothman, C. Hill, R. V. Kochanov, Y. Tan, P. F. Bernath, M. Birk, V. Boudon, A. Campargue, K. V. Chance, B. J. Drouin, J.-M. Flaud, R. R. Gamache, J. T. Hodges, D. Jacquemart, V. I. Perevalov, A. Perrin, K. P. Shine, M. A. H. Smith, J. Tennyson, G. C. Toon, H. Tran, V. G. Tyuterev, A. Barbe, A. G. Császár, V. M. Devi, T. Furtenbacher,

J. J. Harrison, J.-M. Hartmann, A. Jolly, T. J. Johnson, T. Karman, I. Kleiner, A. A. Kyuberis, J. Loos, O. M. Lyulin, S. T. Massie, S. N. Mikhailenko, N. Moazzen-Ahmadi, H. S. P. Müller, O. V. Naumenko, A. V. Nikitin, O. L. Polyansky, M. Rey, M. Rotger, S. W. Sharpe, K. Sung, E. Starikova, S. A. Tashkun, J. V. Auwera, G. Wagner, J. Wilzewski, P. Wcislo, S. Yu, E. J. Zak, The HITRAN2016 molecular spectroscopic database. *J. Quant. Spectrosc. Radiat. Transf.* **203**, 3–69 (2017).

22. G. L. Villanueva, M. J. Mumma, B. P. Bonev, R. E. Novak, R. J. Barber, M. A. DiSanti, Water in planetary and cometary atmospheres: H_2O/HDO transmittance and fluorescence models. *J. Quant. Spectrosc. Radiat. Transf.* **113**, 202–220 (2012).
23. F. Daerden, L. Neary, S. Viscardy, A. García Muñoz, R. T. Clancy, M. D. Smith, T. Encrenaz, A. Fedorova, Mars atmospheric chemistry simulations with the GEM-Mars general circulation model. *Icarus* **326**, 197–224 (2019).
24. L. Neary, F. Daerden, S. Aoki, J. Whiteway, R. T. Clancy, M. Smith, S. Viscardy, J. T. Erwin, I. R. Thomas, G. Villanueva, G. Liuzzi, M. Crismani, M. Wolff, S. R. Lewis, J. A. Holmes, M. R. Patel, M. Giuranna, C. Depiesse, A. Piccialli, S. Robert, L. Trompet, Y. Willame, B. Ristic, A. C. Vandaele, Explanation for the increase in high altitude water on Mars observed by NOMAD during the 2018 global dust storm. *Geophys. Res. Lett.* **47**, e2019GL084354 (2019).
25. E. Millour, F. Forget, A. Spiga, T. Navarro, J.-B. Madeleine, L. Montabone, A. Pottier, F. Lefevre, F. Montmessin, J.-Y. Chaufray, M. A. Lopez-Valverde, F. Gonzalez-Galindo, S. R. Lewis, P. L. Read, J.-P. Huot, M.-C. Desjean; MCD/GCM development Team, The Mars Climate Database (MCD version 5.2). *Eur. Planet. Sci. Congr.* **10**, EPSC2015-438 (2015).
26. B. M. Jakosky, C. B. Farmer, The seasonal and global behavior of water vapor in the Mars atmosphere: Complete global results of the Viking atmospheric water detector experiment. *J. Geophys. Res.* **87**, 2999–3019 (1982).
27. M. D. Smith, Interannual variability in TES atmospheric observations of Mars during 1999–2003. *Icarus* **167**, 148–165 (2004).
28. M. D. Smith, Spacecraft observations of the martian atmosphere. *Annu. Rev. Earth Planet. Sci.* **36**, 191–219 (2008).
29. F. Montmessin, M. D. Smith, Y. Langevin, M. T. Mellon, A. Fedorova, The water cycle. *Atmos. Clim. Mars*, 338–373 (2017).
30. M. D. Smith, F. Daerden, L. Neary, A. Khayat, The climatology of carbon monoxide and water vapor on Mars as observed by CRISM and modeled by the GEM-Mars general circulation model. *Icarus* **301**, 117–131 (2018).
31. A. A. Fedorova, F. Montmessin, O. Korablev, M. Luginin, A. Trokhimovskiy, D. A. Belyaev, N. I. Ignatiev, F. Lefèvre, J. Alday, P. G. J. Irwin, K. S. Olsen, J.-L. Bertaux, E. Millour, A. Määttänen, A. Shakun, A. V. Grigoriev, A. Patrakeev, S. Korsa, N. Kokonkov, L. Baggio, F. Forget, C. F. Wilson, Stormy water on Mars: The distribution and saturation of atmospheric water during the dusty season. *Science* **367**, 297–300 (2020).
32. G. Liuzzi, G. L. Villanueva, M. M. J. Crismani, M. D. Smith, M. J. Mumma, F. Daerden, S. Aoki, A. C. Vandaele, R. T. Clancy, J. Erwin, I. Thomas, B. Ristic, J.-J. Lopez-Moreno, G. Bellucci, M. R. Patel, Strong variability of martian water ice clouds during dust storms revealed from ExoMars Trace Gas Orbiter/NOMAD. *J. Geophys. Res. Planets* **125**, 2019JE006250 (2020).
33. M. S. Chaffin, J. Deighan, N. M. Schneider, A. I. F. Stewart, Elevated atmospheric escape of atomic hydrogen from Mars induced by high-altitude water. *Nat. Geosci.* **10**, 174–178 (2017).
34. B. J. Sandor, R. T. Clancy, HDO in the mesosphere: Observation and modeling of novel isotopic variability. *J. Geophys. Res.* **108**, 4463 (2003).
35. P. N. Blossey, Z. Kuang, D. M. Romps, Isotopic composition of water in the tropical tropopause layer in cloud-resolving simulations of an idealized tropical circulation. *J. Geophys. Res.* **115**, 24309 (2010).
36. A. Gettelman, C. R. Webster, Simulations of water isotope abundances in the upper troposphere and lower stratosphere and implications for stratosphere troposphere exchange. *J. Geophys. Res.* **110**, 17301 (2005).
37. C. Frankenberg, K. Yoshimura, T. Warneke, I. Aben, A. Butz, N. Deutscher, D. Griffith, F. Hase, J. Notholt, M. Schneider, H. Schrijver, T. Rockmann, Dynamic processes governing lower-tropospheric HDO/H_2O Ratios as observed from space and ground. *Science* **325**, 1374–1377 (2009).
38. W. J. Randel, E. Moyer, M. Park, E. Jensen, P. Bernath, K. Walker, C. Boone, Global variations of HDO and HDO/H_2O ratios in the upper troposphere and lower stratosphere derived from ACE-FTS satellite measurements. *J. Geophys. Res. Atmos.* **117**, D06303 (2012).
39. J. J. Plaut, G. Picardi, A. Safaeinili, A. B. Ivanov, S. M. Milkovich, A. Cicchetti, W. Kofman, J. Mouginot, W. M. Farrell, R. J. Phillips, S. M. Clifford, A. Frigeri, R. Orosei, C. Federico, I. P. Williams, D. A. Gurnett, E. Nielsen, T. Hagfors, E. Heggy, E. R. Stofan, D. Plettemeier, T. R. Watters, C. J. Leuschen, P. Edenhofer, Subsurface radar sounding of the south polar layered deposits of Mars. *Science* **316**, 92–95 (2007).
40. M. T. Zuber, D. E. Smith, S. C. Solomon, J. B. Abshire, R. S. Afzal, O. Aharonson, K. Fishbaugh, P. G. Ford, H. V. Frey, J. B. Garvin, J. W. Head, A. B. Ivanov, C. L. Johnson, D. O. Muhleman, G. A. Neumann, G. H. Pettengill, R. J. Phillips, X. Sun, H. J. Zwally, W. B. Banerdt, T. C. Duxbury, Observations of the north polar region of Mars from the Mars orbiter laser altimeter. *Science* **282**, 2053–2060 (1998).
41. J. B. Murray, J.-P. Muller, G. Neukum, S. C. Werner, S. Van Gasselt, E. Hauber, W. J. Markiewicz, J. W. Head III, B. H. Foing, D. Page, K. L. Mitchell, G. Portyankina; HRSC Co-Investigator Team, Evidence from the Mars express high resolution stereo camera for a frozen sea close to Mars' equator. *Nature* **434**, 352–356 (2005).
42. D. P. Page, M. R. Balme, M. M. Grady, Dating martian climate change. *Icarus* **203**, 376–389 (2009).
43. P. H. Smith, L. K. Tamppari, R. E. Arvidson, D. Bass, D. Blaney, W. V. Boynton, A. Carswell, D. C. Catling, B. Clark, T. Duck, E. DeJong, D. Fisher, W. Goetz, H. P. Gunnlaugsson, M. H. Hecht, V. Hipkin, J. Hoffman, S. F. Hviid, H. U. Keller, S. P. Kounaves, C. F. Lange, M. T. Lemmon, M. B. Madsen, W. J. Markiewicz, J. Marshall, C. P. McKay, M. T. Mellon, D. W. Ming, R. V. Morris, W. T. Pike, N. Renno, U. Staufer, C. Stoker, P. Taylor, J. A. Whiteway, A. P. Zent, H_2O at the Phoenix landing site. *Science* **325**, 58–61 (2009).
44. W. V. Boynton, W. C. Feldman, S. W. Squyres, T. H. Prettyman, J. Brückner, L. G. Evans, R. C. Reedy, R. Starr, J. R. Arnold, D. M. Drake, P. A. J. Englert, A. E. Metzger, I. Mitrofanov, J. I. Trombka, C. d'Uston, H. Wänke, O. Gasnault, D. K. Hamara, D. M. Janes, R. L. Marcialis, S. Maurice, I. Mikheeva, G. J. Taylor, R. Tokar, C. Shinohara, Distribution of hydrogen in the near surface of Mars: Evidence for subsurface ice deposits. *Science* **297**, 81–85 (2002).
45. J. Laskar, A. C. M. Correia, M. Gastineau, F. Joutel, B. Levrard, P. Robutel, Long term evolution and chaotic diffusion of the insolation quantities of Mars. *Icarus* **170**, 343–364 (2004).
46. W. Darling, G, A. H. Bath, J. J. Gibson, K. Rozanski, Isotopes in water, in *Isotopes in Palaeoenvironmental Research*, M. J. Leng, Ed. (Springer, 2006), pp. 1–66.
47. A. S. J. Khayat, G. L. Villanueva, M. D. Smith, S. D. Guzewich, IRTF/CSHELL mapping of atmospheric HDO, H_2O and D/H on Mars during northern summer. *Icarus* **330**, 204–216 (2019).
48. T. Encrenaz, C. DeWitt, M. J. Richter, T. K. Greathouse, T. Fouchet, F. Montmessin, F. Lefèvre, B. Bézard, S. K. Atreya, S. Aoki, H. Sagawa, New measurements of D/H on Mars using EXES aboard SOFIA. *Astron. Astrophys.* **612**, A112 (2018).
49. F. Montmessin, T. Fouchet, F. Forget, Modeling the annual cycle of HDO in the Martian atmosphere. *J. Geophys. Res.* **110**, 03006 (2005).
50. F. Daerden, L. Neary, S. Viscardy, S. Aoki, A. Piccialli, S. Robert, V. Wilquet, I. Thomas, B. Ristic, A. Carine Vandaele, G. Villanueva, M. Mumma, R. Novak, T. Encrenaz, S. Lewis, J. Holmes, J. Juan López-Moreno, G. Bellucci, M. Patel, Model expectations for the D/H distribution on Mars as observed by NOMAD. *Eur. Planet. Sci. Congr.* **12**, EPSC2018-742 (2018).
51. R. Hu, Predicted diurnal variation of the deuterium to hydrogen ratio in water at the surface of Mars caused by mass exchange with the regolith. *Earth Planet. Sci. Lett.* **519**, 192–201 (2019).
52. D. Nevejans, E. Neefs, E. Van Ransbeeck, S. Berkenbosch, R. Clairquin, L. De Vos, W. Moelans, S. Glorieux, A. Baeke, O. Korablev, Compact high-resolution spaceborne echelle grating spectrometer with acousto-optical tunable filter based order sorting for the infrared domain from 2.2 to 4.3 μm. *Appl. Optics* **45**, 5191–5206 (2006).
53. A. Mahieux, S. Berkenbosch, R. Clairquin, D. Fussen, N. Mateshvili, E. Neefs, D. Nevejans, B. Ristic, A. C. Vandaele, V. Wilquet, In-flight performance and calibration of SPICAV SOIR onboard Venus Express. *Appl. Optics* **47**, 2252–2265 (2008).
54. M. D. Smith, M. J. Wolff, R. T. Clancy, A. Kleinböhl, S. L. Murchie, Vertical distribution of dust and water ice aerosols from CRISM limb-geometry observations. *J. Geophys. Res. Planets.* **118**, 321–334 (2013).
55. K. Stamnes, G. E. Thomas, J. J. Stamnes, *Radiative Transfer in the Atmosphere and Ocean* (Cambridge Univ. Press, 2017).

Acknowledgments: ExoMars is a space mission of the European Space Agency (ESA) and Roscosmos. The NOMAD experiment is led by the Royal Belgian Institute for Space Aeronomy (IASB-BIRA), assisted by Co-PI teams from Spain (IAA-CSIC), Italy (INAF-IAPS), and the United Kingdom (Open University). **Funding:** This project acknowledges funding by the Belgian Science Policy Office (BELSPO), with the financial and contractual coordination by the ESA Prodex Office (PEA 4000103401 and 4000121493), by the Spanish MICINN through its Plan Nacional, by European funds under grants PGC2018-101836-B-I00 and ESP2017-87143-R (MINECO/FEDER), and by the Spanish Science Ministry Centro de Excelencia Severo Ochoa Program under grant SEV-2017-0709, as well as by the U.K. Space Agency through grants ST/R005761/1, ST/P001262/1, ST/R001405/1, and ST/S00145X/1 and the Italian Space Agency through grant 2018-2-HH.0. This work was supported by NASA's Mars Program Office under WBS 604796, "Participation in the TGO/NOMAD investigation of trace gases on Mars" and by NASA's SEEC initiative under grant number NNX17AH81A, "Remote sensing of planetary atmospheres in the solar system and beyond." M.J.C. was supported by the NASA Postdoctoral Program at the NASA Goddard Space Flight Center, administered by Universities Space Research Association (USRA) under contract with NASA. S.A. is postdoctoral researcher of the Belgian Fund for Scientific Research (FNRS). **Author contributions:** G.L.V. led the investigation and codeveloped the data analysis and retrieval methods. G.L. codeveloped the analysis and retrieval methods. M.J.C., S.A., E.W.K., I.R.T., and M.A.L.-V. supported with the data analysis and

retrieval methods. A.C.V. led the instrument design/characterization and assisted with the retrievals and data interpretation. F.D., M.D.S., M.J.M., L.N., S.V., M.R.P., J.A.H., G.B., and J.J.L.-M. assisted with the overall planning of the investigation and interpretation of the results. B.R. assisted with the mission planning and coordination of the observations. **Competing interests:** The authors declare that they have no competing interests. **Data and materials availability:** All data needed to evaluate the conclusions in the paper are present in the paper and/or the Supplementary Materials. The retrieval package used in this study is the PSG, free and available online at https://psg.gsfc.nasa.gov. Additional data related to this paper may be requested from the authors.

Submitted 19 May 2020
Accepted 2 December 2020
Published 10 February 2021
10.1126/sciadv.abc8843

Citation: G. L. Villanueva, G. Liuzzi, M. M. J. Crismani, S. Aoki, A. C. Vandaele, F. Daerden, M. D. Smith, M. J. Mumma, E. W. Knutsen, L. Neary, S. Viscardy, I. R. Thomas, M. A. Lopez-Valverde, B. Ristic, M. R. Patel, J. A. Holmes, G. Bellucci, J. J. Lopez-Moreno, NOMAD team, Water heavily fractionated as it ascends on Mars as revealed by ExoMars/NOMAD. *Sci. Adv.* **7**, eabc8843 (2021).

Science Advances

Water heavily fractionated as it ascends on Mars as revealed by ExoMars/NOMAD

Geronimo L. Villanueva, Giuliano Liuzzi, Matteo M. J. Crismani, Shohei Aoki, Ann Carine Vandaele, Frank Daerden, Michael D. Smith, Michael J. Mumma, Elise W. Knutsen, Lori Neary, Sebastien Viscardy, Ian R. Thomas, Miguel Angel Lopez-Valverde, Bojan Ristic, Manish R. Patel, James A. Holmes, Giancarlo Bellucci, Jose Juan Lopez-Moreno and NOMAD team

Sci Adv **7** (7), eabc8843.
DOI: 10.1126/sciadv.abc8843

Science Advances (ISSN 2375-2548) is published by the American Association for the Advancement of Science, 1200 New York Avenue NW, Washington, DC 20005. The title *Science Advances* is a registered trademark of AAAS.

Science Advances
AAAS

advances.sciencemag.org/cgi/content/full/7/7/eabc8843/DC1

Supplementary Materials for

Water heavily fractionated as it ascends on Mars as revealed by ExoMars/NOMAD

Geronimo L. Villanueva*, Giuliano Liuzzi, Matteo M. J. Crismani, Shohei Aoki, Ann Carine Vandaele, Frank Daerden, Michael D. Smith, Michael J. Mumma, Elise W. Knutsen, Lori Neary, Sebastien Viscardy, Ian R. Thomas, Miguel Angel Lopez-Valverde, Bojan Ristic, Manish R. Patel, James A. Holmes, Giancarlo Bellucci, Jose Juan Lopez-Moreno, NOMAD team

*Corresponding author. Email: geronimo.villanueva@nasa.gov

Published 10 February 2021, *Sci. Adv.* **7**, eabc8843 (2021)
DOI: 10.1126/sciadv.abc8843

This PDF file includes:

Sections S1 and S2
Figs. S1 to S7
References

S1. Supplementary Material

The NOMAD/TGO spectrometer

The data used in the present study were collected by the Nadir and Occultation for MArs Discovery (NOMAD (*12*, *13*)) instrument operating onboard the ExoMars Trace Gas Orbiter (TGO) 2016, an ESA/ROSCOSMOS joint mission to Mars.

NOMAD is composed of 3 channels: a solar occultation-dedicated channel (SO) operating in the infrared wavelength domain; a second infrared channel mostly used for nadir measurements, but capable also of limb observations (LNO), and an ultraviolet/visible channel (UVIS) that can work in all observation geometries. The spectral resolution of SO and LNO is largely superior to previous surveys in the infrared.

The design of the infrared channels (SO and LNO) is inherited from the SOIR instrument (*52*) developed for the ESA Venus Express mission. SO and LNO design and radiometric characteristics are described in detail in previous works (*12–15*), while a complete calibration using the in-flight data acquired preliminarily to the science phase has been performed and discussed in depth (*16*). ExoMars TGO is in a near-polar orbit, so the NOMAD instrument can ideally perform two occultations per orbit, for a total of 24 occultations per Sol. However, constraints related to the operability of all the instruments onboard TGO limit the number of occultations observed by NOMAD to 12-14 per Sol.

The focus of the present work is on the data acquired by the SO channel, whose routine science operations started in April 2018 and are ongoing. The SO channel operates at wavelengths between 2.2 and 4.3 μm (2325 – 4500 cm^{-1}), using an echelle grating with a groove density of 4 lines/mm in a Littrow configuration, combined with an Acousto-Optic Tunable Filter (AOTF). The AOTF is a narrow bandpass filter, whose transmission properties are tuned using a proper input Radio Frequency that selects the peak wavenumber of the AOTF transfer function, hence the diffraction order that enters the grating + detector system. The width of each order varies from 20 to 35 cm^{-1}, linearly increasing with the diffraction order number. During an occultation, the SO instrument pointed towards the Sun, in order to observe the solar radiation as it is attenuated by the Martian atmosphere at different altitudes, enabling a quasi-punctual investigation of the atmospheric vertical structure. Observations can be performed both in ingress and in egress.

Thanks to the flexibility given by the AOTF of switching between different diffraction orders, measurements consist of rapidly repeated cycles of five or six diffraction orders, whose spectral ranges cover absorption by gases/organics of interest. In this way, at each altitude the instrument provides information about several atmospheric constituents. Limitations in data transmission, and the necessity to increase the signal to noise ratio (SNR), pose a cap to the output number of rows (binned or effective) of the detector to 24. This is the same strategy previously adopted by SOIR (*53*).

The 24 rows of the detector typically image a vertical interval of 7.5 km in tangent height. A single detector row, then, will sample a vertical distance of 500 m. For routine science operations, data are transmitted to Earth in 4 bins, and each of them will add-up the signal of 4 rows in the detector. Depending on the angle between the instrument orbit and the surface of Mars, the atmosphere will be sampled by each bin at intervals between 200 m and 1 km.

Data

For the present study, we have used the Solar Occultations measured by NOMAD between April 2018 (starting of science operations) and April 2019. This corresponds to the temporal interval LS 162.5 of MY34 and LS 15.0 of MY35, for a total of 1,920 occultations, and more than 1 million spectra analyzed. The data used correspond to data Level 0.3, version 1.0 of the data provided by the NOMAD PI institute (nomad.aeronomie.be).

In spite of their punctual spatial coverage, occultations are taken throughout every latitude and longitude of the globe, permitting both the investigation of local phenomena, and the derivation of general latitude vs. time global trend at all altitudes.

Among the five or six orders measured during an occultation, there is always at least one order in which water vapor absorption lines are visible. In 90% of the occultations, however, water vapor can be retrieved from 2 or more independent diffraction orders, and HDO from one of them, allowing quantification of the D/H for almost all NOMAD occultations. The detail about the diffraction orders used to derive H_2O and HDO is illustrated in Figure S1. Orders 121, 134 and 168 are measured the most frequently (in 80% of the occultations) and include lines from $2\nu_2$ and ν_3 water bands.

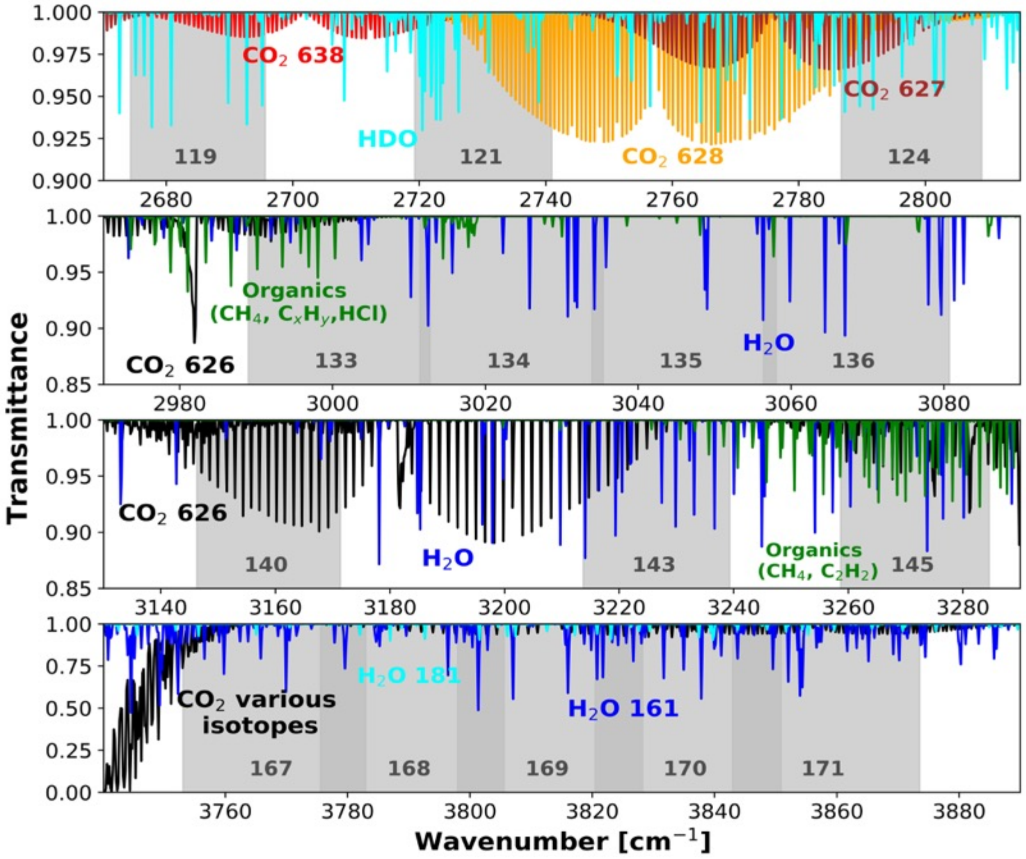

Figure S1. The plot summarizes the average transmittance of the Martian atmosphere in Solar Occultation geometry at h=20 km, with the assumption of an aerosol-free atmosphere. Isotopic bands for CO_2 and H_2O are evidenced in different colors, while organics absorption is shown in green. The grey patches show the position and spectral coverage of each of the diffraction orders observed by NOMAD that are used in the present study. In particular, they encompass water lines of different opacities, and the strong HDO Q-branch at 2720 cm^{-1}.

The possibility to access different absorption bands for water is of great benefit to achieve measurement accuracy throughout a vast range of altitudes, since absorption regimes are varying with the observed atmospheric column. During an occultation, NOMAD observes atmospheric integrated water columns that are much larger than in Nadir geometry; for low altitudes, this implies that the observed spectral lines will be typically saturated, posing some challenges in the interpretation of retrieved water abundances. On the other hand, when observing the upper atmosphere, the apparent water column will be still high enough to observe water lines above the instrumental noise level in the stronger ν_3 band; typically, these stronger lines allow to quantify the water main isotope abundance at altitudes up to 100-105 km. This concept is better shown in Figure S2, where we report the curve of growth of two spectral lines in the two bands covered by NOMAD. The combination of water measurements in different ro-vibrational bands is of great importance to ensure robustness of the results and richness of information on the entire vertical profile.

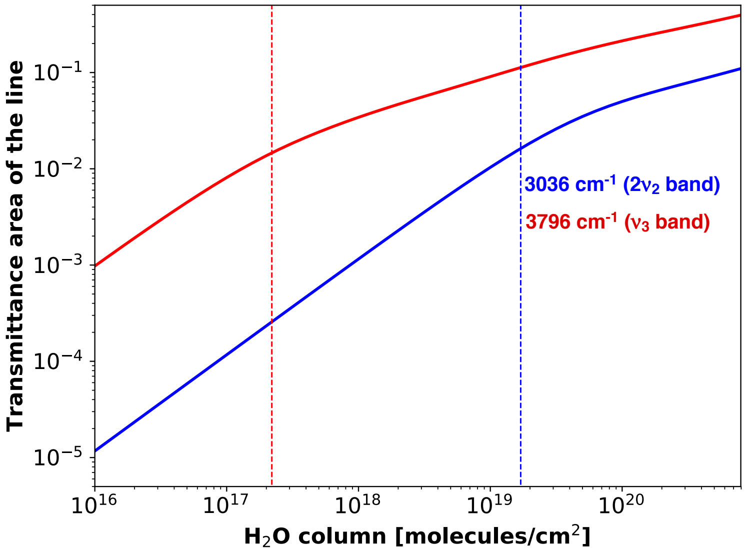

Figure S2. The figure shows the different behavior of the curve of growth of two lines in the $2\nu_2$ *and* ν_3 *bands of* H_2O*. The weaker* $2\nu_2$ *band lines reach saturation (dashed vertical lines) for water columns (x-axis) much larger than the lines in the* ν_3 *band, and there is between 1 and 2 orders of magnitude of difference between the opacities of the two lines considered.*

Data pre-processing

As already stated, the radiation intensity observed by NOMAD is the result of a convolution between the incident flux on the instrument, and the spectral functions describing both the AOTF transmittance and the grating (i.e. the Blaze function (*16*)). For these reasons, data are pre-processed prior to retrieval. The spectra used in this study correspond to data Level 0.3, version 1.0 of the data provided by the NOMAD PI institute (nomad.aeronomie.be).

The initial step consists in computing the transmittance for each observed order and altitude, from surface to the Top Of Atmosphere (TOA), along the line of sight. Those spectra acquired by NOMAD at altitudes at which no atmospheric absorption is visible (above the TOA) provide the reference spectra, F, and the signal intensity is modeled only by Blaze function and AOTF. Each spectrum below the TOA, which we indicate with I, is divided by an average of a subset of reference spectra *F*. If both *I* and *F* signal intensities are in unit of observed photons, the calculation of transmittance τ and related uncertainty σ_τ is as follows:

$$\tau = \frac{I}{F} \tag{1}$$

$$\sigma_\tau = \tau\sqrt{\left(\frac{\sigma_I}{I}\right)^2 + \left(\frac{\sigma_F}{F}\right)^2} \tag{2}$$

In the reasonable hypothesis that, among the many possible causes of noise, the dominant one is the one due to the intensity of the source (Sun as a point source), the uncertainties σ_I and σ_F are computed as the square root of the signal itself:

$$\sigma_I = \sqrt{I};\ \sigma_F = \frac{1}{\sqrt{N}}\sqrt{\sum\nolimits_{j=1,\dots,N} F_j} \tag{3}$$

with *N* the number of reference spectra.

The choice of the set of reference spectra $\{F_j\}_{j=1,\dots,N}$ is critical to correctly compute transmittances minimizing the systematics. A major source of such effects are the temperature variations during an occultation, which can be as large as a few K, and that cause two different effects. The first consists in micro-misalignments between the pixel-to-wavenumber relation of the reference spectra and the observed spectrum[6]. This yields to dispersion features in the derived transmittance, in correspondence of solar lines, whose amplitude is sometimes comparable to atmospheric absorption features, especially at high altitudes, and can significantly degrade the signal-to-noise ratio calculated with the uncertainties in Eq. (**3**). The second effect is the shift of the center of the AOTF spectral response function, which is again related to thermal-induced micro-deformations of the AOTF crystal. This usually results in artifacts in the transmittance continuum, which fluctuates around its average value with variations as large as a few percent. Both these issues are resolved and properly taken into account during the actual retrieval process (see Section Retrieval).

To mitigate these issues, the altitude at which the $\{F_j\}_{j=1,\dots,N}$ spectra are located is chosen as closest as possible to the TOA, and *N* is limited to make them fall in an altitude range < 20 km. This is based on the fact that the instrument temperature varies however slowly compared to the time needed to perform a six order measurement cycle (~1 second).

The definition of the TOA varies with the diffraction order. In fact, for the sake of normalization, the TOA is related to the altitude at which atmospheric absorption is no longer detected, which depends on the spectral interval observed. Different TOA definitions have been adopted in differing spectral intervals: for orders 119 to 136, (figure S1), the TOA is located at 120 km (where no molecular absorption is detectable); for orders 140 to 145 and 167 to 171, at 140 km.

A schematic view of a NOMAD data sample and their normalization is provided in Figure S3, where it is also shown how water lines visibility at different altitudes differs among orders. During the retrieval process, we utilize transmittances derived from single spectra, in order to maximize the vertical sampling of the vertical profile, and to minimize biases deriving potentially arising from spectral binning (such as micro-misalignment between the frequency of consecutive spectra).

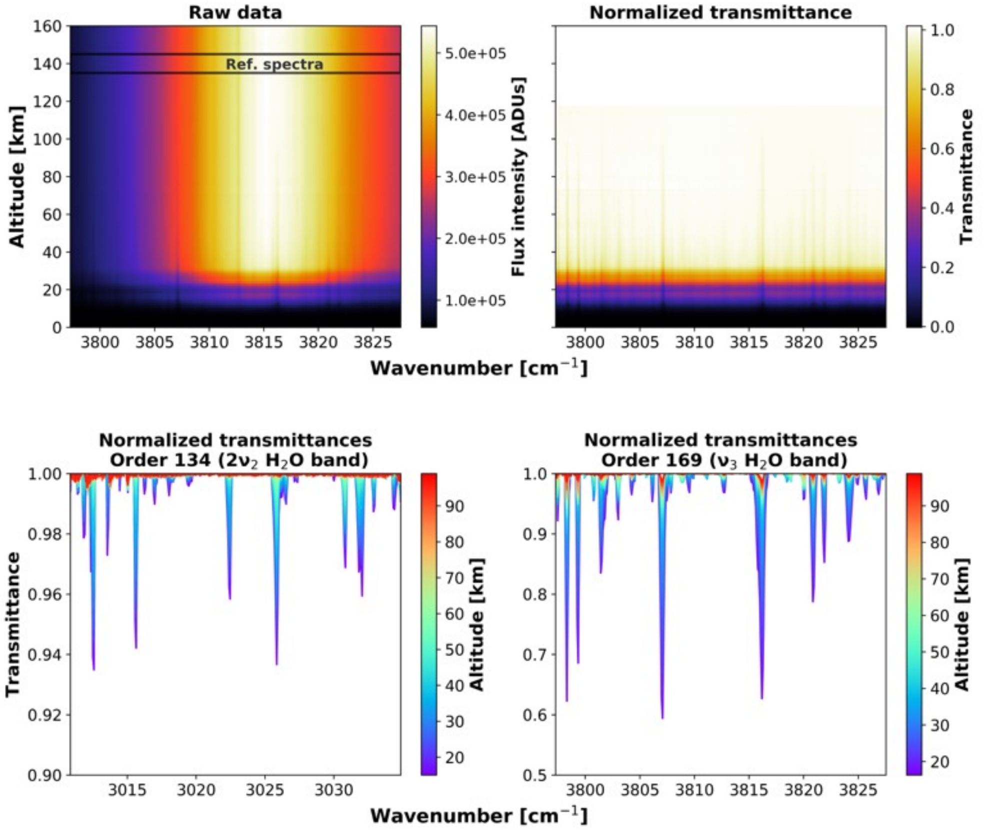

Figure S3: Top: The left plot shows an example of the raw signal as it is acquired by NOMAD SO (order 169). The signal is the result of convolution between the blaze function and the order mixing due to the AOTF filter. Each row represents the spectrum observed at a specific altitude, as it results from binning the signal of each of the illuminated rows of the detector. The location of the reference spectra (outside the atmospheric absorption) is evidenced. Right: derived transmittance, once the original signal is divided by the average of the reference spectra. Bottom: two examples of normalized transmittances in orders 134 (left) and 169 (right) from the same occultation (data acquired simultaneously). All the spectra are divided by their average continuum, to highlight only the molecular absorption as it varies across different altitudes (shown by colors). It is easy to notice the difference in line depth between the two orders, as discussed previously.

Retrieval methodology

Retrievals are performed using the Planetary Spectrum Generator (PSG (*17*)), and is based on an Optimal Estimation approach (*18*), modified with an extra regularization parameter (*19*, *20*). PSG is an online radiative transfer tool capable of synthesizing planetary spectra (atmosphere + surface) in a vast range of wavelengths (0.1 μm to 100 mm) from any observatory (e.g. JWST, ALMA), orbiter (e.g., Cassini, TGO), or lander (e.g., MSL, InSight). This is achieved by integrating many state-of-art radiative transfer codes and existing knowledge, spectral databases, and planetary climate and circulation models.

The radiative transfer relies on the most up-to-date spectral line compilations, in particular the newly released HITRAN 2016 database (*54*). In the case of Mars, for water and its isotopologues, PSG ingests a specific line compilation tailored on a CO_2-rich atmosphere (*22*). Radiative transfer can be computed either via line-by-line calculations, or using a faster kcorrelated approach, and the high spectral resolution of NOMAD requires full line-by-line calculations. PSG is able to perform multiple scattering from atmospheric aerosols, using the discrete ordinates method (*55*, *56*). PSG is able to ingest also a plethora of optical constants from different types of aerosols, adaptable to Earth and many other planetary bodies, Mars included. However, for the present investigation, we do not retrieve aerosols, nor we use the multiple scattering capabilities of the tool, since the observation geometry implies that the scattering contribution to the total observed flux is negligible, even in presence of aerosols along the line of sight (point-source).

During the retrieval process, every measurement is considered independent of the others. While, in principle, each observation probes all the atmospheric layers from the tangent altitude up to the TOA, it has been verified that ~80% of the observed column is representative of the atmospheric state at the tangent altitude. Therefore, we consider each measurement independent, and the retrieved profile is the natural result of the values retrieved at each altitude.

Input parameters and a-priori

For each spectrum, depending on the wavenumber range covered, we retrieved the abundance, in terms of relative volume abundance on the observed column (ppv). In most cases, this corresponds only to retrieve the sole H_2O or HDO abundance, and in some cases (orders 119-124 and 140-167) also the CO_2 column. As a consequence, the retrieved values will be largely dependent upon the assumptions made about the vertical structure of the atmosphere in terms of p-T profile, which determines the density of the observed column [molecules m^{-2}].

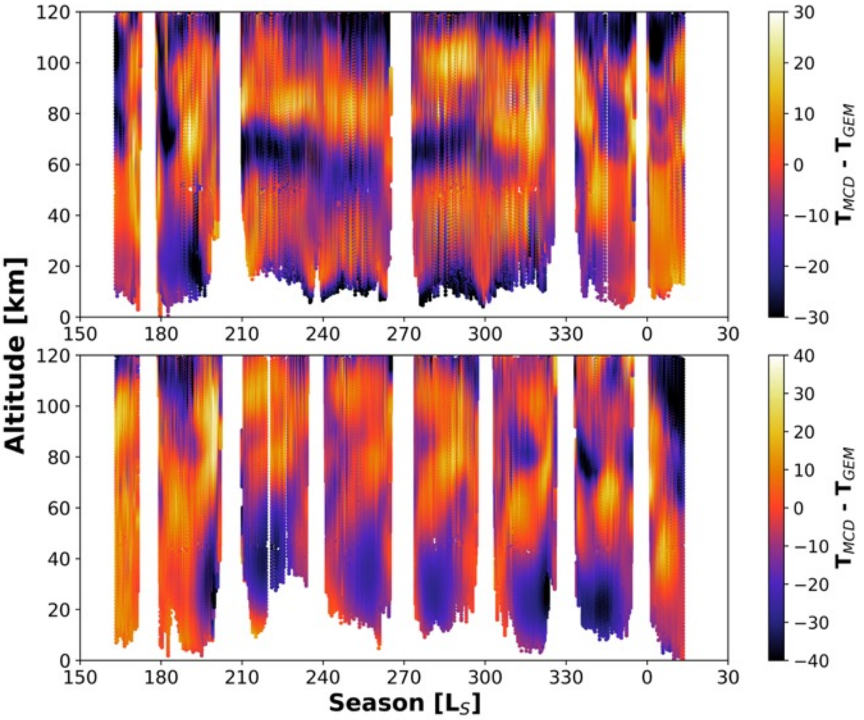

Figure S4. The temperatures as described by the Mars Climate Database (MCD) and the GEM models, collocated with NOMAD occultations, show discrepancies as large as ~10 K in many cases, in both hemispheres (Upper panel: N; lower panel: S). The largest differences (~30 K) occur at L_S *200 to 220, corresponding to the most intense phase of the*

GDS, and are caused by the fact that GEM includes an accurate description of the GDS itself, while MCD does not.

As described in the main section, the atmospheric density can vary during perihelion season, depending on the intensity of the heating effect due to the amount of dust present in the atmosphere. Since the dataset we analyzed is acquired during a Global Dust Storm (GDS), the a-priori atmospheric state has to be representative of those specific conditions, and it is calculated using the GEM-Mars model that uses a specific dust-storm scenario that correctly reproduces the thermal state of the atmosphere during MY34. Retrievals ingest the input provided by GEM-Mars with a temporal sampling of 4 hours, and 51 atmospheric layers from the surface to 150 km of altitude. The deviations of GEM-Mars GDS scenario from the average climatology of Mars Climate Database(*25*) (MCD, v5.2) are significant during the storm, and can be as large as 30 K in temperature in the middle atmosphere (figure S4). The largest discrepancies are found in the S hemisphere, where dust concentration is larger during the GDS. While such differences have a limited impact on those values retrieved by observation of low-J lines, such as HDO and H_2O ν_3 bands (fig. S1), they can strongly influence retrievals from high-J lines (H_2O $2\nu_2$ band), which constitute a large portion of the total retrievals performed.

Instrument effects: AOTF and thermal perturbations

As briefly described before, the radiation observed by NOMAD is the result of a complex superposition of wavelengths and diffraction orders determined by the AOTF filter. Thus, the assessment of its properties and variability is necessary to correctly simulate actual NOMAD observations.

The way in which the AOTF transfer function is modeled, and how it combines radiation coming from different wavelengths into the same spectrum is described in detail in previous works(*16*), and is currently implemented in PSG. Because the AOTF transfer function can be simplified by a sinc squared, whose width is comparable to the wavenumber range of a single diffraction order, the AOTF will combine the radiation coming from the central and nearby orders. In general, a portion of the flux between 50% and 90% is actually due to the central order, while the complementary fraction is related to nearby orders. Prior to retrievals, we have conducted a preliminary investigation to determine how many nearby orders are needed to confidently retrieve water vapor and CO_2 from NOMAD observations minimizing the bias.

An example of the impact of the number of orders is shown in Figure S5 for order 169, together with the order contribution intensities. While the value of the observed water column can be assessed even with a limited (two) number of nearby orders, the uncertainties and the χ^2 improve significantly only including a considerable amount of nearby orders in the simulations. This experiment has been replicated for all the orders used to retrieve water vapor and HDO, to determine the optimal number of orders to include in the calculations.

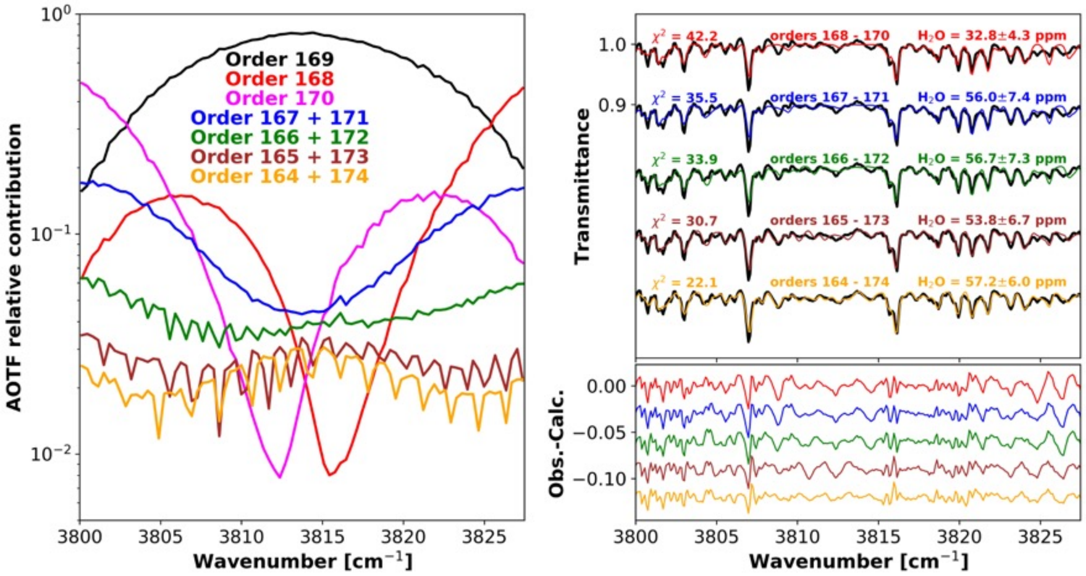

Figure S5: Left: example of contribution to the total observed flux in order 169. Right: example of H_2O abundance retrieval from order 169. The quality of retrieval and residuals improves as an increasing number of orders is included in the calculation. To correctly reproduce all the observed spectral features, 5 adjacent orders on both sides need to be included.

Besides the number of orders to be included, the retrieval assumes an a-priori value for the wavenumber at which the AOTF function is centered. Figure S5 shows that even a small shift in the center of the AOTF function can modify the contribution functions from each order, and then the apparent depth of spectral lines and the retrieved water values. In order to minimize the uncertainty related to this parameter, we have conducted a quantitative analysis of the AOTF center variability with diffraction order and instrument temperature. While the general relationship has been determined in previous works (*16*), the retrievals have also taken into account the temperature-induced shift of the AOTF center, which has been found to vary order by order (from ~0.17 cm^{-1}/K for order 121, to ~0.25 cm^{-1}/K for order 169).

Other instrumental effects, such as small deviations of the wavenumber-to-pixel relation from the theoretical expectation are accounted during the fitting process, as the frequency calibration is determined at each step of the Optimal Estimation process. Eventual residual dispersion features arising from a non-complete solar spectrum subtraction, due to frequency calibration shifts, are subtracted during the fitting process as well.

Spectra selection and noise limitation strategy

To limit the number of noisy measurements, we have excluded all those measurements whose continuum transmittance is below the 5% level. This value corresponds to excluding all those measurements with a single spectrum-Signal to Noise Ratio (SNR) <~100, since at the TOA the SNR varies between 2000 and 3000, depending on the diffraction order (*15*). This threshold on the transmittance excludes most of the data acquired by NOMAD at altitudes < 5 km, and during the most intense phase of the GDS excludes almost all the measurements below 25 km. In principle, in the lower atmosphere, a better SNR could be achieved by binning a certain number of consecutive spectra, however this can heavily degrade the spectral resolution, because of the above mentioned frequency solution displacements between one spectrum and the next one. For this reason the approach adopted is to simply disregard low-signal spectra, and not to perform any average.

With the exception of those diffraction orders situated in the core of the CO_2 absorption ($v_1 + v_3$), the continuum intensity is mainly determined by water ice and dust aerosols along the line of sight. No explicit dust and/or water ice retrieval is performed simultaneously with H_2O, CO_2 and HDO; instead, the spectral continuum (whose slope(s) are also related to AOTF shifts) is fitted with a 5th degree polynomial at every step of the Optimal Estimation, and subtracted. This does not affect the gases retrieval, since the measurements are taken in absorption, and scattering is negligible.

Order combination and dataset creation

The combination of retrieved H_2O and HDO abundances is not trivial, since it requires taking into account both the sensitivity of each measurement (and the above mentioned saturation issues) and the actual statistical uncertainty provided by Optimal Estimation. Regarding the first issue, however, the radiative transfer scheme used within retrievals is able to take into account and correctly compute line absorption in saturated conditions; furthermore, the calculation of uncertainties in the context of Optimal Estimation is weighted against the Jacobians, i.e. the derivatives of the observed signal w.r.t. the retrieved parameter(s), which reflects eventual line saturation. Therefore, to combine different measurements and obtain one single vertical profile for each gas and occultation, we work under the hypothesis that their uncertainties reflect both the signal radiometric uncertainty, and the actual spectroscopic sensitivity of the measurement to the retrieved parameter.

For each occultation, the number of retrievals of water vapor abundances (one for each order sensitive to water vapor absorption) varies between n=2 and n=5. To compute a single water profile per each occultation, measurements are first collected to form a single dataset; then:

- Collocated in time, finding m indices, denoted with ***J**, of* water vapor retrievals $\{Q_i\}_{i=1,\ldots,m}$ belonging to the same occultation, by filtering their acquisition time;
- Clustered in altitude, finding groups of n retrievals, each located at the same altitude: $\{Q_{i\in J}\}_{i=1,\ldots,n}$;
- Averaging the $\{Q_{i\in J}\}_{i=1,\ldots,n}$ found at each altitude, using the corresponding uncertainties $\{\sigma_{i\in J}\}_{i=1,\ldots,n}$.

Under the assumption (see previously) that measurements at different altitudes are independent of each other, the value of water vapor and its uncertainty will be:

$$Q = \frac{\sum_{i=1}^{n} \frac{Q_i}{\sigma_i}}{\sum_{i=1}^{n} \frac{1}{\sigma_i}} \tag{4}$$

$$\sigma_Q = \frac{\sqrt{n}}{\sum_{i=1}^{n} \frac{1}{\sigma_i}} \tag{5}$$

The same operation is performed for HDO, where typically 1 to 3 measurements are available at each altitude in a single occultation. The D/H ratio is finally determined using the same approach: for each occultation and altitude, the D/H is computed using the weighted averages of H_2O and HDO.

The main benefit of aggregating water measurements in this way is to enhance the sensitivity of the retrievals at all the altitudes, exploiting the variety of absorption regimes (saturated vs. non saturated lines) encountered during an occultation, from the surface to the TOA. In Figure S6, we show all the H_2O retrievals from order 134 and 168, and the respective statistical uncertainties. In the retrieved abundances plot, values whose uncertainty is above 15 ppm are not represented.

The water abundances retrieved from different spectral bands look consistent throughout most of the vertical and seasonal coverage. Inconsistencies are found during the most intense phase of the GDS, between L_S 200 and 220, and at altitudes between 20 and 40 km at many temporal instances. In both cases, this is due to the high water column, which yields saturation of the water lines in order 168, leading to a difference in sensitivity between the two orders. Order 134, instead, is effectively dominated by noise rather than line saturation, and as a consequence the retrieval uncertainty increases dramatically over 60 km, where H_2O lines drop below the noise level.

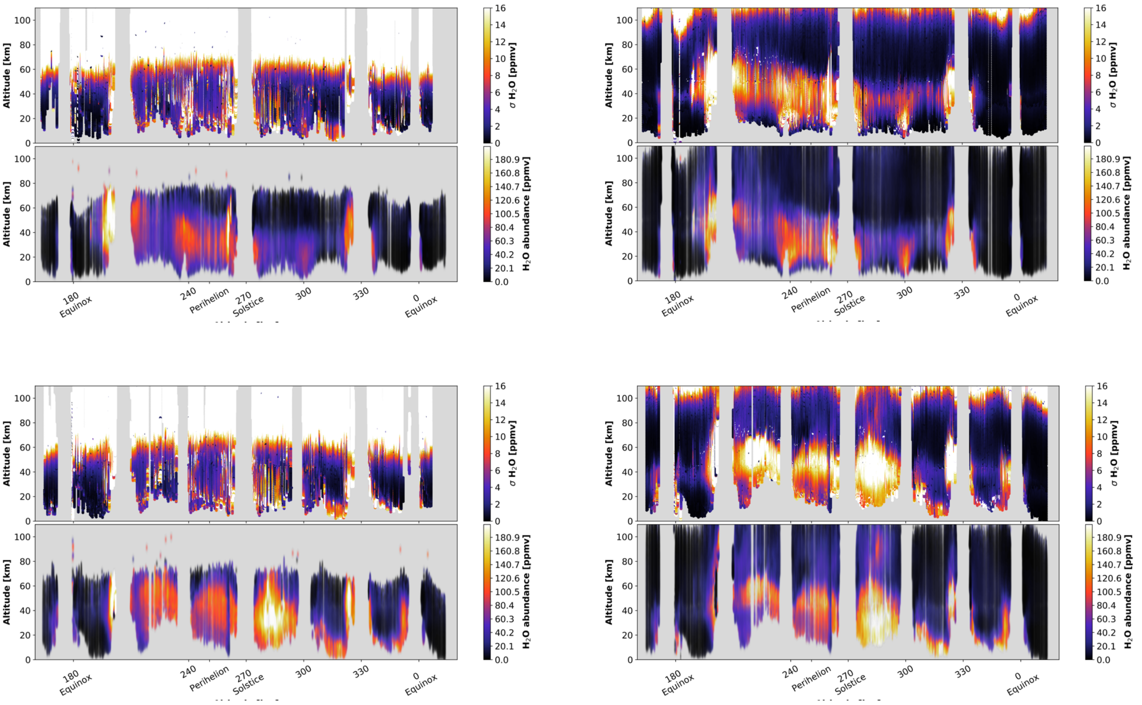

Figure S6. Left: uncertainty of the retrieved values of water vapor from order 134 and actual retrievals. NH is on the top, SH on the bottom. Right: same, for order 168. The latter is sensitive to water vapor up to 100 km, differently from 134, which provides reliable water retrievals up to 60 km. The SNR of order 168 varies with altitude, and reveals that there are 3 different altitude ranges corresponding to different saturation regimes of the lines in the ν_3 band.

Uncertainties of H_2O, HDO and D/H profiles

In each of the derived profiles of H_2O and HDO, the statistical uncertainty of each point (resulting from the combination of *n* retrievals) is expressed by Eq. (5). To quantify the statistical uncertainty of the D/H profile, we can use the basic error propagation for a ratio of two quantities. The combined uncertainties for the final H_2O and D/H profiles are shown in Figure S7 for the two hemispheres.

It can be noticed that the combined uncertainty on H_2O is lower than the single order uncertainties reported in Figure S6, as expected: because a weighted average is performed, the upper atmosphere will essentially be described by the retrievals performed on the stronger water lines, while in the mid to lower atmosphere, the final error will reflect mostly the values obtained by analyzing optically thin lines. This improvement is reflected in the uncertainty affecting D/H as well, where lines are always optically thin, and they will provide information up to 40 km (low water column) to 65 km (GDS-like situation, high water column).

At lower altitudes (< 20 km), however, the actual uncertainty affecting the D/H ratio can be higher, since the biases between the water retrieved from optically thin and thick lines can be significantly larger than the statistical uncertainty of each single-order measurement. In these cases, the actual dispersion of the single order profiles can be as large as 30%, reflecting in an equal error on the derived D/H. Nevertheless, the statistical errors calculated via Optimal Estimation reflect part of the uncertainty related to this aspect, and the combination of retrievals from different orders, even if dispersed, is an effective way to take into account the information content correctly.

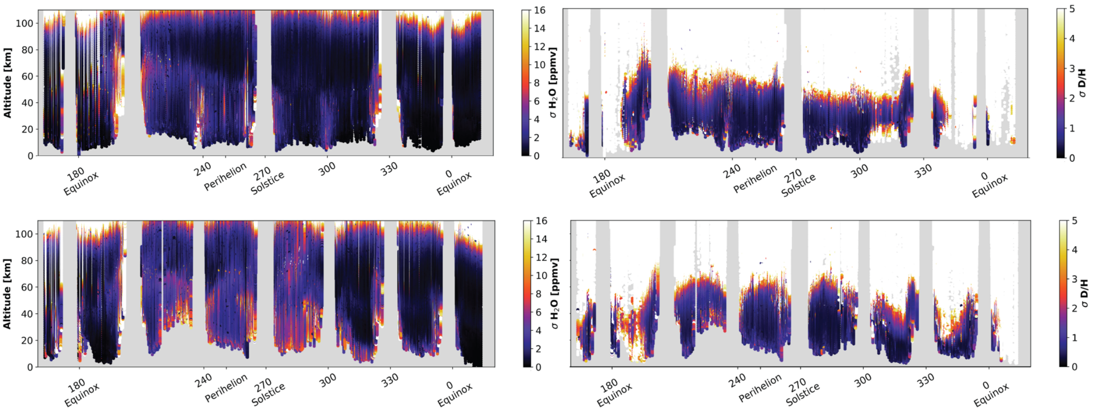

Figure S7. Top left: combined final uncertainty for the H_2O in the NH. Top right: combined final uncertainty for the derived D/H profiles. The sharp transition between values <2 and above 5 coincides with the maximum altitude at which HDO is detected. Bottom panels: same as top for the retrievals in the SH.

S2. NOMAD team

The NOMAD science team is composed by: Vandaele, Ann Carine; Lopez Moreno, Jose Juan; Bellucci, Giancarlo; Patel, Manish; Altieri, Francesca; Aoki, Shohei; Bauduin, Sophie; Bolsée, David; Carrozzo, Giacomo; Clancy, Todd; Cloutis, Edward; Crismani, Matteo; Daerden, Frank; Da Pieve, Fabiana; D'Aversa, Emiliano; Depiesse, Cédric; Erwin, Justin; Etiope, Giuseppe; Fedorova, Anna; Funke, Bernd; Fussen, Didier; Garcia-Comas, Maia; Gérard, Jean-Claude; Gkouvelis, Leo; Giuranna, Marco; Gonzalez-Galindo, Francisco; Hewson, Will; Holmes, James; Hubert, Benoît; Ignatiev, Nicolai; Kaminski, Jacek; Karatekin, Ozgur; Kasaba, Yasumasa; Kass, David, Kleinböhl, Armin; Lanciano, Orietta; Lefèvre, Franck; Lewis, Stephen; Liuzzi, Giulano; López-Puertas, Manuel; López-Valverde, Miguel; Mahieux, Arnaud; Mason, Jon; Mège, Daniel; Mumma, Mike; Nakagawa, Hiromu, Neary, Lori; Neefs, Eddy; Novak, Rob; Oliva, Fabrizio; Piccialli, Arianna; Renotte, Etienne; Ritter, Birgit; Robert, Severine; Rosenblatt, Pascal; Schmidt, Frédéric; Schneider, Nick; Sindoni, Giuseppe; Smith, Michael D.; Teanby, Nicholas A.; Thiemann, Ed; Thomas, Ian; Trokhimovskiy, Alexander; Vander Auwera, Jean; Villanueva, Geronimo; Viscardy, Sébastien; Whiteway, Jim; Willame, Yannick; Wilquet, Valérie; Wolff, Michael; Wolkenberg, Paulina; Yelle, Roger.

REFERENCES AND NOTES

1. M. H. Carr, J. W. Head III, Oceans on Mars: An assessment of the observational evidence and possible fate. *J. Geophys. Res.* **108**, 5042 (2003).

2. A. G. Fairén, A cold and wet Mars. *Icarus* **208**, 165–175 (2010).

3. J. M. Davis, M. Balme, P. M. Grindrod, R. M. E. Williams, S. Gupta, Extensive Noachian fluvial systems in Arabia Terra: Implications for early Martian climate. *Geology* **44**, 847–850 (2016).

4. K. M. Cannon, S. W. Parman, J. F. Mustard, Primordial clays on Mars formed beneath a steam or supercritical atmosphere. *Nature* **552**, 88–91 (2017).

5. G. L. Villanueva, M. J. Mumma, R. E. Novak, H. U. Käufl, P. Hartogh, T. Encrenaz, A. Tokunaga, A. Khayat, M. D. Smith, Strong water isotopic anomalies in the martian atmosphere: Probing current and ancient reservoirs. *Science* **348**, 218–221 (2015).

6. D. Fisher, R. E. Novak, M. J. Mumma, D/H ratio during the northern polar summer and what the Phoenix mission might measure. *J. Geophys. Res.* **113**, E00A15 (2008).

7. R. E. Novak, M. J. Mumma, G. L. Villanueva, Measurement of the isotopic signatures of water on Mars; implications for studying methane. *Planet. Space Sci.* **59**, 163–168 (2011).

8. A. C. Vandaele, J. J. López-Moreno, M. R. Patel, G. Bellucci, F. Daerden, R. Drummond, E. Neefs, S. Robert, J. Rodriguez Gomez, NOMAD, a spectrometer suite for nadir and solar occultation observations on the ExoMars Trace Gas Orbiter. *EGU Gen. Assem. 2012* **14**, 3362 (2012).

9. A. C. Vandaele, O. Korablev, F. Daerden, S. Aoki, I. R. Thomas, F. Altieri, M. López-Valverde, G. Villanueva, G. Liuzzi, M. D. Smith, J. T. Erwin, L. Trompet, A. A. Fedorova, F. Montmessin, A. Trokhimovskiy, D. A. Belyaev, N. I. Ignatiev, M. Luginin, K. S. Olsen, L. Baggio, J. Alday, J.-L. Bertaux, D. Betsis, D. Bolsée, R. T. Clancy, E. Cloutis, C. Depiesse, B. Funke, M. Garcia-Comas, J.-C. Gérard, M. Giuranna, F. Gonzalez-Galindo, A. V. Grigoriev, Y. S. Ivanov, J. Kaminski, O. Karatekin, F. Lefèvre, S. Lewis, M. López-Puertas, A. Mahieux, I. Maslov, J. Mason, M. J. Mumma, L. Neary, E. Neefs, A. Patrakeev, D. Patsaev, B. Ristic, S. Robert, F. Schmidt, A. Shakun, N. A.

Teanby, S. Viscardy, Y. Willame, J. Whiteway, V. Wilquet, M. J. Wolff, G. Bellucci, M. R. Patel, J.-J. López-Moreno, F. Forget, C. F. Wilson, H. Svedhem, J. L. Vago, D. Rodionov; NOMAD Science Team; ACS Science Team, Martian dust storm impact on atmospheric H_2O and D/H observed by ExoMars Trace Gas Orbiter. *Nature* **568**, 521–525 (2019).

10. S. Aoki, A. C. Vandaele, F. Daerden, G. L. Villanueva, G. Liuzzi, I. R. Thomas, J. T. Erwin, L. Trompet, S. Robert, L. Neary, S. Viscardy, R. T. Clancy, M. D. Smith, M. A. Lopez-Valverde, B. Hill, B. Ristic, M. R. Patel, G. Bellucci, J.-J. Lopez-Moreno; NOMAD Team, Water vapor vertical profiles on Mars in dust storms observed by TGO/NOMAD. *J. Geophys. Res. Planets* **124**, 3482–3497 (2019).

11. O. Korablev, F. Montmessin, A. Trokhimovskiy, A. A. Fedorova, A. V. Shakun, A. V. Grigoriev, B. E. Moshkin, N. I. Ignatiev, F. Forget, F. Lefèvre, K. Anufreychik, I. Dzuban, Y. S. Ivanov, Y. K. Kalinnikov, T. O. Kozlova, A. Kungurov, V. Makarov, F. Martynovich, I. Maslov, D. Merzlyakov, P. P. Moiseev, Y. Nikolskiy, A. Patrakeev, D. Patsaev, A. Santos-Skripko, O. Sazonov, N. Semena, A. Semenov, V. Shashkin, A. Sidorov, A. V. Stepanov, I. Stupin, D. Timonin, A. Y. Titov, A. Viktorov, A. Zharkov, F. Altieri, G. Arnold, D. A. Belyaev, J. L. Bertaux, D. S. Betsis, N. Duxbury, T. Encrenaz, T. Fouchet, J.-C. Gérard, D. Grassi, S. Guerlet, P. Hartogh, Y. Kasaba, I. Khatuntsev, V. A. Krasnopolsky, R. O. Kuzmin, E. Lellouch, M. A. Lopez-Valverde, M. Luginin, A. Määttänen, E. Marcq, J. Martin Torres, A. S. Medvedev, E. Millour, K. S. Olsen, M. R. Patel, C. Quantin-Nataf, A. V. Rodin, V. I. Shematovich, I. Thomas, N. Thomas, L. Vazquez, M. Vincendon, V. Wilquet, C. F. Wilson, L. V. Zasova, L. M. Zelenyi, M. P. Zorzano, The Atmospheric Chemistry Suite (ACS) of three spectrometers for the ExoMars 2016 trace gas orbiter. *Space Sci. Rev.* **214**, 7 (2018).

12. A. C. Vandaele, E. Neefs, R. Drummond, I. R. Thomas, F. Daerden, J.-J. Lopez-Moreno, J. Rodriguez, M. R. Patel, G. Bellucci, M. Allen, F. Altieri, D. Bolsée, T. Clancy, S. Delanoye, C. Depiesse, E. Cloutis, A. Fedorova, V. Formisano, B. Funke, D. Fussen, A. Geminale, J.-C. Gérard, M. Giuranna, N. Ignatiev, J. Kaminski, O. Karatekin, F. Lefèvre, M. López-Puertas, M. López-Valverde, A. Mahieux, J. McConnell, M. Mumma, L. Neary, E. Renotte, B. Ristic, S. Robert, M. Smith, S. Trokhimovsky, J. V. Auwera, G. Villanueva, J. Whiteway, V. Wilquet, M. Wolff, Science objectives and performances of NOMAD, a spectrometer suite for the ExoMars TGO mission. *Planet. Space Sci.* **119**, 233–249 (2015).

13. A. C. Vandaele, J.-J. Lopez-Moreno, M. R. Patel, G. Bellucci, F. Daerden, B. Ristic, S. Robert, I. R. Thomas, V. Wilquet, M. Allen, G. Alonso-Rodrigo, F. Altieri, S. Aoki, D. Bolsée, T. Clancy, E. Cloutis, C. Depiesse, R. Drummond, A. Fedorova, V. Formisano, B. Funke, F. González-Galindo, A. Geminale, J.-C. Gérard, M. Giuranna, L. Hetey, N. Ignatiev, J. Kaminski, O. Karatekin, Y. Kasaba, M. Leese, F. Lefèvre, S. R. Lewis, M. López-Puertas, M. López-Valverde, A. Mahieux, J. Mason, J. McConnell, M. Mumma, L. Neary, E. Neefs, E. Renotte, J. Rodriguez-Gomez, G. Sindoni, M. Smith, A. Stiepen, A. Trokhimovsky, J. Vander Auwera, G. Villanueva, S. Viscardy, J. Whiteway, Y. Willame, M. Wolff, NOMAD, an integrated suite of three spectrometers for the ExoMars trace gas mission: Technical description, science objectives and expected performance. *Space Sci. Rev.* **214**, 80 (2018).

14. E. Neefs, A. C. Vandaele, R. Drummond, I. R. Thomas, S. Berkenbosch, R. Clairquin, S. Delanoye, B. Ristic, J. Maes, S. Bonnewijn, G. Pieck, E. Equeter, C. Depiesse, F. Daerden, E. V. Ransbeeck, D. Nevejans, J. Rodriguez-Gómez, J.-J. López-Moreno, R. Sanz, R. Morales, G. P. Candini, M. C. Pastor-Morales, B. A. del Moral, J.-M. Jeronimo-Zafra, J. M. Gómez-López, G. Alonso-Rodrigo, I. Pérez-Grande, J. Cubas, A. M. Gomez-Sanjuan, F. Navarro-Medina, T. Thibert, M. R. Patel, G. Bellucci, L. De Vos, S. Lesschaeve, N. V. Vooren, W. Moelans, L. Aballea, S. Glorieux, A. Baeke, D. Kendall, J. De Neef, A. Soenen, P.-Y. Puech, J. Ward, J.-F. Jamoye, D. Diez, A. Vicario-Arroyo, M. Jankowski, NOMAD spectrometer on the ExoMars trace gas orbiter mission: Part 1—Design, manufacturing and testing of the infrared channels. *Appl. Optics* **54**, 8494–8520 (2015).

15. I. R. Thomas, A. C. Vandaele, S. Robert, E. Neefs, R. Drummond, F. Daerden, S. Delanoye, B. Ristic, S. Berkenbosch, R. Clairquin, J. Maes, S. Bonnewijn, C. Depiesse, A. Mahieux, L. Trompet, L. Neary, Y. Willame, V. Wilquet, D. Nevejans, L. Aballea, W. Moelans, L. De Vos, S. Lesschaeve, N. Van Vooren, J.-J. Lopez-Moreno, M. R. Patel, G. Bellucci; NOMAD Team, Optical and radiometric models of the NOMAD instrument part II: The infrared channels – SO and LNO. *Opt. Express* **24**, 3790–3805 (2016).

16. G. Liuzzi, G. L. Villanueva, M. J. Mumma, M. D. Smith, F. Daerden, B. Ristic, I. Thomas, A. C. Vandaele, M. R. Patel, J.-J. Lopez-Moreno, G. Bellucci, Methane on Mars: New insights into the sensitivity of CH4 with the NOMAD/ExoMars spectrometer through its first in-flight calibration. *Icarus* **321**, 671–690 (2019).

17. G. L. Villanueva, M. D. Smith, S. Protopapa, S. Faggi, A. M. Mandell, Planetary spectrum generator: An accurate online radiative transfer suite for atmospheres, comets, small bodies and exoplanets. *J. Quant. Spectrosc. Radiat. Transf.* **217**, 86–104 (2018).

18. C. D. Rodgers, *Inverse Methods for Atmospheric Sounding* (series on Atmospheric, Oceanic and Planetary Physics, World Scientific, 2000); www.worldscientific.com/worldscibooks/10.1142/3171.

19. G. Liuzzi, G. Masiello, C. Serio, S. Venafra, C. Camy-Peyret, Physical inversion of the full IASI spectra: Assessment of atmospheric parameters retrievals, consistency of spectroscopy and forward modelling. *J. Quant. Spectrosc. Radiat. Transf.* **182**, 128–157 (2016).

20. A. Carissimo, I. De Feis, C. Serio, The physical retrieval methodology for IASI: The δ-IASI code. *Environ. Model. Software* **20**, 1111–1126 (2005).

21. I. E. Gordon, L. S. Rothman, C. Hill, R. V. Kochanov, Y. Tan, P. F. Bernath, M. Birk, V. Boudon, A. Campargue, K. V. Chance, B. J. Drouin, J.-M. Flaud, R. R. Gamache, J. T. Hodges, D. Jacquemart, V. I. Perevalov, A. Perrin, K. P. Shine, M. A. H. Smith, J. Tennyson, G. C. Toon, H. Tran, V. G. Tyuterev, A. Barbe, A. G. Császár, V. M. Devi, T. Furtenbacher, J. J. Harrison, J.-M. Hartmann, A. Jolly, T. J. Johnson, T. Karman, I. Kleiner, A. A. Kyuberis, J. Loos, O. M. Lyulin, S. T. Massie, S. N. Mikhailenko, N. Moazzen-Ahmadi, H. S. P. Müller, O. V. Naumenko, A. V. Nikitin, O. L. Polyansky, M. Rey, M. Rotger, S. W. Sharpe, K. Sung, E. Starikova, S. A. Tashkun, J. V. Auwera, G. Wagner, J. Wilzewski, P. Wcislo, S. Yu, E. J. Zak, The HITRAN2016 molecular spectroscopic database. *J. Quant. Spectrosc. Radiat. Transf.* **203**, 3–69 (2017).

22. G. L. Villanueva, M. J. Mumma, B. P. Bonev, R. E. Novak, R. J. Barber, M. A. DiSanti, Water in planetary and cometary atmospheres: H_2O/HDO transmittance and fluorescence models. *J. Quant. Spectrosc. Radiat. Transf.* **113**, 202–220 (2012).

23. F. Daerden, L. Neary, S. Viscardy, A. García Muñoz, R. T. Clancy, M. D. Smith, T. Encrenaz, A. Fedorova, Mars atmospheric chemistry simulations with the GEM-Mars general circulation model. *Icarus* **326**, 197–224 (2019).

24. L. Neary, F. Daerden, S. Aoki, J. Whiteway, R. T. Clancy, M. Smith, S. Viscardy, J. T. Erwin, I. R. Thomas, G. Villanueva, G. Liuzzi, M. Crismani, M. Wolff, S. R. Lewis, J. A. Holmes, M. R. Patel, M. Giuranna, C. Depiesse, A. Piccialli, S. Robert, L. Trompet, Y. Willame, B. Ristic, A. C. Vandaele, Explanation for the increase in high altitude water on Mars observed by NOMAD during the 2018 global dust storm. *Geophys. Res. Lett.* **47**, e2019GL084354 (2019).

25. E. Millour, F. Forget, A. Spiga, T. Navarro, J.-B. Madeleine, L. Montabone, A. Pottier, F. Lefevre, F. Montmessin, J.-Y. Chaufray, M. A. Lopez-Valverde, F. Gonzalez-Galindo, S. R. Lewis, P. L. Read, J.-P. Huot, M.-C. Desjean; MCD/GCM development Team, The Mars Climate Database (MCD version 5.2). *Eur. Planet. Sci. Congr.* **10**, EPSC2015-438 (2015).

26. B. M. Jakosky, C. B. Farmer, The seasonal and global behavior of water vapor in the Mars atmosphere: Complete global results of the Viking atmospheric water detector experiment. *J. Geophys. Res.* **87**, 2999–3019 (1982).

27. M. D. Smith, Interannual variability in TES atmospheric observations of Mars during 1999–2003. *Icarus* **167**, 148–165 (2004).

28. M. D. Smith, Spacecraft observations of the martian atmosphere. *Annu. Rev. Earth Planet. Sci.* **36**, 191–219 (2008).

29. F. Montmessin, M. D. Smith, Y. Langevin, M. T. Mellon, A. Fedorova, The water cycle. *Atmos. Clim. Mars* 338–373 (2017).

30. M. D. Smith, F. Daerden, L. Neary, A. Khayat, The climatology of carbon monoxide and water vapor on Mars as observed by CRISM and modeled by the GEM-Mars general circulation model. *Icarus* **301**, 117–131 (2018).

31. A. A. Fedorova, F. Montmessin, O. Korablev, M. Luginin, A. Trokhimovskiy, D. A. Belyaev, N. I. Ignatiev, F. Lefèvre, J. Alday, P. G. J. Irwin, K. S. Olsen, J.-L. Bertaux, E. Millour, A. Määttänen, A. Shakun, A. V. Grigoriev, A. Patrakeev, S. Korsa, N. Kokonkov, L. Baggio, F. Forget, C. F. Wilson, Stormy water on Mars: The distribution and saturation of atmospheric water during the dusty season. *Science* **367**, 297–300 (2020).

32. G. Liuzzi, G. L. Villanueva, M. M. J. Crismani, M. D. Smith, M. J. Mumma, F. Daerden, S. Aoki, A. C. Vandaele, R. T. Clancy, J. Erwin, I. Thomas, B. Ristic, J.-J. Lopez-Moreno, G. Bellucci, M. R. Patel, Strong variability of martian water ice clouds during dust storms revealed from ExoMars Trace Gas Orbiter/NOMAD. *J. Geophys. Res. Planets* **125**, 2019JE006250 (2020).

33. M. S. Chaffin, J. Deighan, N. M. Schneider, A. I. F. Stewart, Elevated atmospheric escape of atomic hydrogen from Mars induced by high-altitude water. *Nat. Geosci.* **10**, 174–178 (2017).

34. B. J. Sandor, R. T. Clancy, HDO in the mesosphere: Observation and modeling of novel isotopic variability. *J. Geophys. Res.* **108**, 4463 (2003).

35. P. N. Blossey, Z. Kuang, D. M. Romps, Isotopic composition of water in the tropical tropopause layer in cloud-resolving simulations of an idealized tropical circulation. *J. Geophys. Res.* **115**, 24309 (2010).

36. A. Gettelman, C. R. Webster, Simulations of water isotope abundances in the upper troposphere and lower stratosphere and implications for stratosphere troposphere exchange. *J. Geophys. Res.* **110**, 17301 (2005).

37. C. Frankenberg, K. Yoshimura, T. Warneke, I. Aben, A. Butz, N. Deutscher, D. Griffith, F. Hase, J. Notholt, M. Schneider, H. Schrijver, T. Rockmann, Dynamic processes governing lower-tropospheric HDO/H_2O Ratios as observed from space and ground. *Science* **325**, 1374–1377 (2009).

38. W. J. Randel, E. Moyer, M. Park, E. Jensen, P. Bernath, K. Walker, C. Boone, Global variations of HDO and HDO/H_2O ratios in the upper troposphere and lower stratosphere derived from ACE-FTS satellite measurements. *J. Geophys. Res. Atmos.* **117**, D06303 (2012).

39. J. J. Plaut, G. Picardi, A. Safaeinili, A. B. Ivanov, S. M. Milkovich, A. Cicchetti, W. Kofman, J. Mouginot, W. M. Farrell, R. J. Phillips, S. M. Clifford, A. Frigeri, R. Orosei, C. Federico, I. P. Williams, D. A. Gurnett, E. Nielsen, T. Hagfors, E. Heggy, E. R. Stofan, D. Plettemeier, T. R. Watters, C. J. Leuschen, P. Edenhofer, Subsurface radar sounding of the south polar layered deposits of Mars. *Science* **316**, 92–95 (2007).

40. M. T. Zuber, D. E. Smith, S. C. Solomon, J. B. Abshire, R. S. Afzal, O. Aharonson, K. Fishbaugh, P. G. Ford, H. V. Frey, J. B. Garvin, J. W. Head, A. B. Ivanov, C. L. Johnson, D. O. Muhleman, G. A. Neumann, G. H. Pettengill, R. J. Phillips, X. Sun, H. J. Zwally, W. B. Banerdt, T. C. Duxbury, Observations of the north polar region of Mars from the Mars orbiter laser altimeter. *Science* **282**, 2053–2060 (1998).

41. J. B. Murray, J.-P. Muller, G. Neukum, S. C. Werner, S. Van Gasselt, E. Hauber, W. J. Markiewicz, J. W. Head III, B. H. Foing, D. Page, K. L. Mitchell, G. Portyankina, HRSC Co-Investigator Team, Evidence from the Mars express high resolution stereo camera for a frozen sea close to Mars' equator. **434**, 352–356 (2005).

42. D. P. Page, M. R. Balme, M. M. Grady, Dating martian climate change. *Icarus* **203**, 376–389 (2009).

43. P. H. Smith, L. K. Tamppari, R. E. Arvidson, D. Bass, D. Blaney, W. V. Boynton, A. Carswell, D. C. Catling, B. Clark, T. Duck, E. DeJong, D. Fisher, W. Goetz, H. P. Gunnlaugsson, M. H. Hecht, V. Hipkin, J. Hoffman, S. F. Hviid, H. U. Keller, S. P. Kounaves, C. F. Lange, M. T. Lemmon, M. B. Madsen, W. J. Markiewicz, J. Marshall, C. P. McKay, M. T. Mellon, D. W. Ming, R. V. Morris, W. T. Pike, N. Renno, U. Staufer, C. Stoker, P. Taylor, J. A. Whiteway, A. P. Zent, H_2O at the Phoenix landing site. *Science* **325**, 58–61 (2009).

44. W. V. Boynton, W. C. Feldman, S. W. Squyres, T. H. Prettyman, J. Brückner, L. G. Evans, R. C. Reedy, R. Starr, J. R. Arnold, D. M. Drake, P. A. J. Englert, A. E. Metzger, I. Mitrofanov, J. I. Trombka, C. d'Uston, H. Wänke, O. Gasnault, D. K. Hamara, D. M. Janes, R. L. Marcialis, S. Maurice, I. Mikheeva, G. J. Taylor, R. Tokar, C. Shinohara, Distribution of hydrogen in the near surface of Mars: Evidence for subsurface ice deposits. *Science* **297**, 81–85 (2002).

45. J. Laskar, A. C. M. Correia, M. Gastineau, F. Joutel, B. Levrard, P. Robutel, Long term evolution and chaotic diffusion of the insolation quantities of Mars. *Icarus* **170**, 343–364 (2004).

46. W. Darling, G, A. H. Bath, J. J. Gibson, K. Rozanski, Isotopes in water, in *Isotopes in Palaeoenvironmental Research*, M. J. Leng, Ed. (Springer, 2006), pp. 1–66.

47. A. S. J. Khayat, G. L. Villanueva, M. D. Smith, S. D. Guzewich, IRTF/CSHELL mapping of atmospheric HDO, H_2O and D/H on Mars during northern summer. *Icarus* **330**, 204–216 (2019).

48. T. Encrenaz, C. DeWitt, M. J. Richter, T. K. Greathouse, T. Fouchet, F. Montmessin, F. Lefèvre, B. Bézard, S. K. Atreya, S. Aoki, H. Sagawa, New measurements of D/H on Mars using EXES aboard SOFIA. *Astron. Astrophys.* **612**, A112 (2018).

49. F. Montmessin, T. Fouchet, F. Forget, Modeling the annual cycle of HDO in the Martian atmosphere. *J. Geophys. Res.* **110**, 03006 (2005).

50. F. Daerden, L. Neary, S. Viscardy, S. Aoki, A. Piccialli, S. Robert, V. Wilquet, I. Thomas, B. Ristic, A. Carine Vandaele, G. Villanueva, M. Mumma, R. Novak, T. Encrenaz, S. Lewis, J. Holmes, J. Juan López-Moreno, G. Bellucci, M. Patel, Model expectations for the D/H distribution on Mars as observed by NOMAD. *Eur. Planet. Sci. Congr.* **12**, EPSC2018-742 (2018).

51. R. Hu, Predicted diurnal variation of the deuterium to hydrogen ratio in water at the surface of Mars caused by mass exchange with the regolith. *Earth Planet. Sci. Lett.* **519**, 192–201 (2019).

52. D. Nevejans, E. Neefs, E. Van Ransbeeck, S. Berkenbosch, R. Clairquin, L. De Vos, W. Moelans, S. Glorieux, A. Baeke, O. Korablev, Compact high-resolution spaceborne echelle grating spectrometer with acousto-optical tunable filter based order sorting for the infrared domain from 2.2 to 4.3 μm. *Appl. Optics* **45**, 5191–5206 (2006).

53. A. Mahieux, S. Berkenbosch, R. Clairquin, D. Fussen, N. Mateshvili, E. Neefs, D. Nevejans, B. Ristic, A. C. Vandaele, V. Wilquet, In-flight performance and calibration of SPICAV SOIR onboard Venus Express. *Appl. Optics* **47**, 2252–2265 (2008).

54. M. D. Smith, M. J. Wolff, R. T. Clancy, A. Kleinböhl, S. L. Murchie, Vertical distribution of dust and water ice aerosols from CRISM limb-geometry observations. *J. Geophys. Res. Planets.* **118**, 321–334 (2013).

55. K. Stamnes, G. E. Thomas, J. J. Stamnes, *Radiative Transfer in the Atmosphere and Ocean* (Cambridge Univ. Press, 2017).